doi:10.26443/seismica.v5i1.2254

The Influence of Shallow Subsurface Properties on Particle Motion in Acoustic–Seismic Coupling

Logan T. Scamfer * [1], **David Fee** [1], **Jordan W. Bishop** [2], **Matthew Haney** [3], **Kenneth Macpherson** [1]

[1]Wilson Alaska Technical Center, Geophysical Institute, University of Alaska Fairbanks, Fairbanks, AK, USA, [2]Los Alamos National Laboratory, Los Alamos, NM, USA, [3]United States Geological Survey, Alaska Volcano Observatory, Anchorage, AK, USA

Author contributions: *Conceptualization*: Logan Scamfer, David Fee, Jordan Bishop, Matthew Haney, Kenneth Macpherson. *Methodology*: Logan Scamfer, David Fee, Jordan Bishop, Matthew Haney, Kenneth Macpherson. *Formal Analysis*: Logan Scamfer. *Writing - Original draft*: Logan Scamfer. *Writing - Review & Editing*: Logan Scamfer, David Fee, Jordan Bishop, Matthew Haney, Kenneth Macpherson. *Project administration*: David Fee.

Production Editor:
Yen Joe Tan
Handling Editor:
Oliver Lamb
Copy & Layout Editor:
Théa Ragon

Received:
December 11, 2025
Accepted:
April 29, 2026
Published:
May 26, 2026

Abstract Atmospheric acoustic waves transmit energy into the solid Earth through air-to-ground coupling. These waves are recorded by seismic sensors and provide insight into both atmospheric phenomena and subsurface properties. Interpreting these signals is often challenging because they are modulated by subsurface structure and the incidence angle of the acoustic wave. This study examines acoustic–seismic coupling generated by the 2012 Camp Minden Explosion, which was recorded by hundreds of seismoacoustic stations. We apply a novel technique to quantify the seismic particle motion, model coupled waves with a propagator matrix approach, and apply a Bayesian inversion to infer properties of the shallow subsurface. Our analysis reveals that prograde motion is widespread and focused in low shear-wave velocity regions, such as the Mississippi Embayment, and retrograde motion is more common in higher shear-velocity areas. Inversion results at some stations produce plausible subsurface models with strong waveform fits, while inversions at other sites are less successful. These results indicate prograde particle motion in air-to-ground coupled waves is more prevalent than previously recognized and may serve as a diagnostic for shallow velocity structure. Our comprehensive modeling and inversion framework provides a potential method to extract layered near-surface properties from acoustic–seismic coupling observations.

1 Introduction

When low-frequency acoustic (infrasound) waves impinge on the Earth's surface, they can couple into the solid Earth and produce ground motion measurable on seismometers. These signals are often referred to as air-to-ground coupled waves (AGCWs) or ground-coupled airwaves (GCAs). Within the seismoacoustics community, AGCWs are increasingly recognized as a valuable tool for studying energetic acoustic sources, including volcanoes (De Angelis et al., 2012; Ichihara et al., 2012; Fee et al., 2016), anthropogenic explosions (Anthony et al., 2022b; Wills et al., 2022), meteors (Hicks et al., 2023; Walker et al., 2010), and aircraft (Wang et al., 2024; Seppi et al., 2025). In addition to characterizing atmospheric sources, AGCWs carry information about the elastic properties of the subsurface, and studies have demonstrated the potential to infer these properties (Novoselov et al., 2020; Macpherson et al., 2025; Langston, 2004).

AGCWs can provide insight into both the acoustic source and the subsurface, but interpretation can be challenging because the observed ground motions are highly sensitive to subsurface structure. This shallow structure can be complex and is often poorly constrained. Characteristics of the seismic particle motion are particularly important: they are used to identify AGCWs and to inform methods that estimate the back-azimuth of the incident infrasound wave (Bishop et al., 2023; Langston, 2004), and these methods often rely on the assumption of retrograde elliptical motion. Simplified and widely used theoretical models of acoustic–seismic coupling predict retrograde motion (Ben-Menahem and Singh, 1981; Sorrells, 1971), yet observations indicate the conditions producing prograde particle motion are more common than expected (Langston, 2004; Novoselov et al., 2020). Understanding how subsurface properties influence these deviations is a key focus of this study.

Correlations between atmospheric pressure perturbations and recordings of seismic ground motion have long been observed (Crary and Ewing, 1952; Ewing and Press, 1953; Press and Ewing, 1951). Some early studies attributed this phenomenon to the buoyant response of seismometer mass to ambient pressure changes, but Haubrich and MacKenzie (1965) showed that an effect persists even when seismometers are isolated in near-vacuum conditions, indicating that elastic deformation plays a role. Sorrells (1971) derived transfer functions for a plane-wave pressure perturbation (e.g., wind) horizontally propagating over a homogeneous, isotropic, elastic halfspace. This case is often referred to as static loading. A key assumption in this theory is that the pres-

*Corresponding author: ltscamfer@alaska.edu

sure perturbations have a phase velocity c much less than the shear-wave velocity β of the halfspace. Ben-Menahem and Singh (1981) extended this theory to incident acoustic waves, and showed an equivalence between Sorrells' theory and the acoustic wave case if the phase velocity c is replaced by the apparent acoustic velocity $\hat{c}$. Similarly, the theory of Ben-Menahem and Singh (1981) shares the key assumption that $\hat{c} \ll \beta$. For an acoustic pressure perturbation P_0 with apparent velocity $\hat{c}$, energy is predicted to couple into only the radial component U_x (in the direction of the incident wave) and vertical U_z seismic component:

$$U_x = \frac{-i\hat{c}P_0}{2\omega(\lambda+\mu)} e^{i\omega(t-x/\hat{c})}, \tag{1}$$

$$U_z = \frac{-\hat{c}P_0}{2\omega(\lambda+\mu)} \left(\frac{\lambda+2\mu}{\mu}\right) e^{i\omega(t-x/\hat{c})}. \tag{2}$$

where λ is Lamé's first parameter, μ is the shear modulus of the solid halfspace, x is the horizontal position, i is the imaginary unit, t is time, and ω is the angular frequency.

The ratio of vertical to horizontal displacement of these coupled waves is therefore

$$\frac{U_z}{U_x} = \left(\frac{\lambda+2\mu}{\mu}\right) e^{-i\pi/2}. \tag{3}$$

Equation 3 contains a prediction that is relevant to our study: the vertical displacement is phase-delayed by $\frac{\pi}{2}$ relative to the radial displacement, and the vertical amplitude is at least twice as great. In other words, the pressure-induced ground motions have retrograde elliptical particle motion. As previously mentioned, this characteristic is widely assumed and commonly used to identify AGCWs (Anthony et al., 2022b; Berg et al., 2022; Wills et al., 2022). However, observations of prograde AGCWs have also been reported (Langston, 2004; Novoselov et al., 2020), motivating theoretical analysis (Bishop et al., 2022). Unlike the earlier treatments of Sorrells (1971) and Ben-Menahem and Singh (1981), which assume $\hat{c} \ll \beta$, Bishop et al. (2022) considered the regime where the apparent acoustic velocity $\hat{c}$ is greater than the subsurface shear-wave velocity β. For a homogeneous halfspace, they showed that the sense of particle motion transitions from retrograde to prograde, and the elliptical motion becomes tilted when $\hat{c} > \sqrt{2}\beta$. These findings highlight that AGCW particle motions are highly dependent on subsurface velocity structure and the apparent acoustic velocity. Consequently, interpretation of particle motions requires considering the pressure source type (acoustic wave or wind), the wave incidence angle, and the subsurface structure.

One application of AGCWs that motivates this study is the ability to estimate an infrasound back-azimuth at stations having co-located acoustic and seismic sensors. Traditionally, infrasound arrays and beamforming algorithms are used to determine the direction of incoming acoustic waves (Szuberla and Olson, 2004; Cansi, 1995). However, recent approaches leverage the seismic response recorded by three-component seismometers to estimate the back-azimuth (Bishop et al., 2023; McKee et al., 2018). These methods provide an opportunity to expand infrasound detection capabilities around the world, requiring far fewer sensors and a much smaller geographic footprint. Unlike dedicated infrasound arrays, seismic stations are far more abundant, and the addition of a single infrasound sensor could enable directional analysis at those sites. In fact, stations of the temporary EarthScope USArray Transportable Array installed after 2011 included co-located seismic and acoustic sensors, and some have since been adopted permanently. Similarly, many stations in the Global Seismographic Network (GSN; Albuquerque Seismological Laboratory/USGS, 1988) have also added infrasound sensors. While the recent Transverse Coherence Minimization (TCM) method (Bishop et al., 2023) is powerful, it inherits a key assumption about AGCWs from earlier theory: the seismic particle motion is retrograde elliptical. This assumption stems from previously mentioned theoretical models of acoustic–seismic coupling (Ben-Menahem and Singh, 1981; Sorrells, 1971) and is used to resolve a 180° back-azimuth ambiguity inherent to the TCM method. This problem is analogous to back-azimuth determination for purely seismic Rayleigh waves, which are typically retrograde but may also be prograde (Tanimoto and Rivera, 2005). While the retrograde assumption can often hold, our study demonstrates that prograde AGCW particle motion occurs frequently. Recognizing and characterizing when this occurs is critical for applying seismoacoustic back-azimuth methods at broader scales to avoid incorrect directional analyses. As an example, particle motion analysis was required to inform TCM back-azimuth estimates of acoustic signals from the 2023 eruption of Shishaldin Volcano, Alaska (Fee et al., in press).

Another important application of AGCWs is probing the elastic properties of the subsurface. Tanimoto and Wang (2018) first estimated near-surface rigidity (upper 50–100 m) using colocated seismic and pressure instruments, with wind as the pressure source (Sorrells, 1971). Subsequent studies (Tanimoto and Wang, 2020; Wang and Tanimoto, 2020) extended this framework by comparing coupling-derived estimates of V_{S30} (the subsurface shear-wave velocity of the upper 30 m) with active-source seismic estimates and models based on proxies such as topographic slope (Heath et al., 2020). While these studies considered wind as the driving pressure perturbation, they established the basis for applying the Ben-Menahem and Singh (1981) model, which assumes acoustic waves as the pressure source. Studies that use acoustic sources have been applied in widely different scenarios. Edwards et al. (2007) leveraged infrasound from the 2006 Stardust sample return capsule to assess the theory of Ben-Menahem and Singh (1981), using a subsurface model informed by a seismic refraction survey and measurements of soil properties. Very shallow depths ($<$ 5 m) have also been explored using active-source seismoacoustic experiments; for instance, Novoselov et al. (2020) derived Lamé parameters (λ and μ) and Poisson's ratio in the uppermost layer using firecrackers as a source and a setup of co-located acoustic sensors and nodal seismometers. At the other end of the scale, highly energetic infrasound from the 2022 eruption of Hunga volcano in Tonga has been used

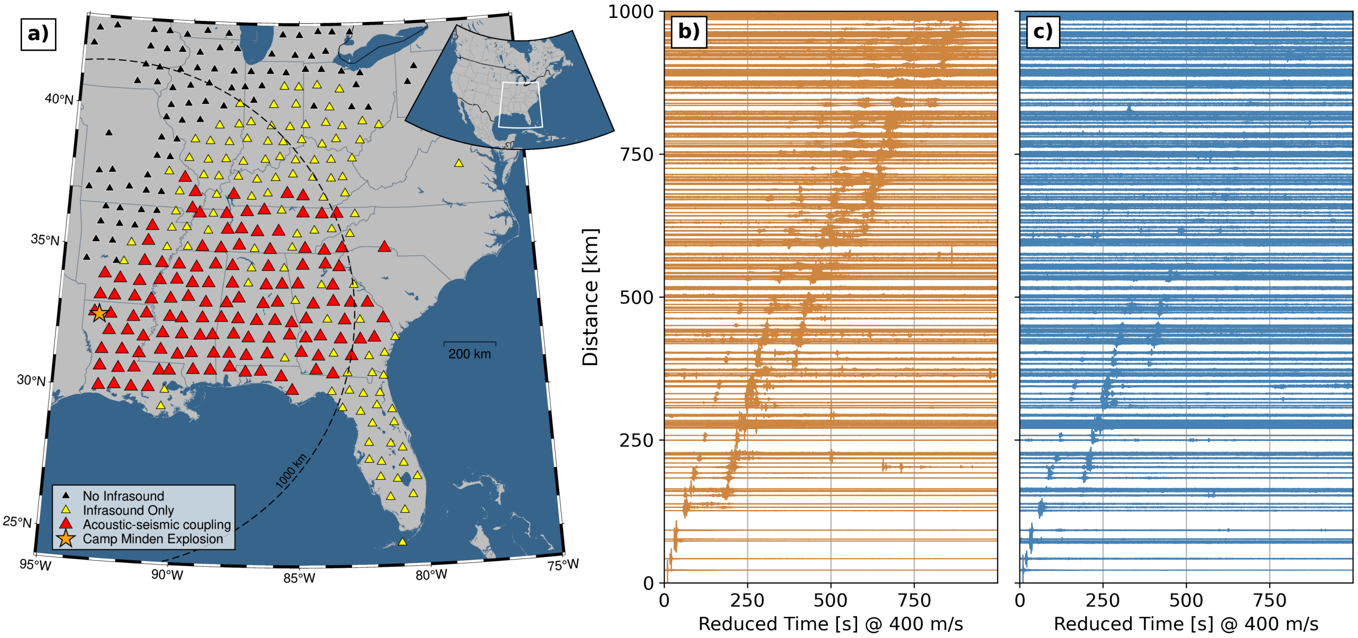

Figure 1 Camp Minden seismoacoustic signals. **a)** Map of EarthScope Transportable Array stations that recorded signals from the Camp Minden Explosion. Red triangles denote stations with recorded air-to-ground coupled waves (126), yellow stations only recorded infrasound signals (240), and black stations received no signal. The dashed line encircling the location of the explosion (orange star) encloses stations whose waveforms are shown in the record sections in the following panels. **b)** Acoustic and **c)** seismic record sections of seismoacoustic signatures from the 2012 Camp Minden Explosion, out to 1000 km from the source. Waveforms are normalized and filtered 0.8–4 Hz.

to estimate elasticity structure up to several kilometers depth (Anthony et al., 2022a; Macpherson et al., 2025).

These existing approaches have targeted bulk Earth properties such as rigidity or shear-wave velocity, but constraining shallow, layered subsurface structure using acoustic waves remains largely unexplored. To address this, we reevaluate some assumptions in Ben-Menahem and Singh (1981). Specifically, we consider a model that has more complexity than a halfspace, and we relax the high velocity contrast assumption between the atmosphere and solid Earth. While the velocity assumption holds well in Sorrells (1971) (as the pressure source is wind, which is likely much slower than subsurface shear-wave speeds), the apparent velocity of an acoustic wave can often exceed shallow subsurface velocities (Liu et al., 1997; Romero and Rix, 2001; Mori et al., 2020). Additionally, observations of prograde AGCW particle motion and the explanation for such phenomenon in Bishop et al. (2022) highlight the need to address this assumption.

To examine these conditions, a more flexible acoustic–seismic coupling framework is needed. Such flexibility is provided by propagator matrix methods, which have long been used to model seismic waves propagating through layered media (Haskell, 1953; Harkrider and Flinn, 1970). Langston (2004), for example, applied this method with a multilayered subsurface to explain seismic signals generated by coupling of infrasound from a bolide. More recently, Xu and Lognonné (2024) extended this approach to model coupling on Mars by combining the propagator matrix with eigenfunction theory (Aki and Richards, 2002), yielding a comprehensive forward-modeling framework that encompasses both static loading (Sorrells, 1971) and acoustic wave incidence (Ben-Menahem and Singh, 1981). This method constructs acoustic–seismic transfer functions, referred to as compliance, which describe the frequency-dependent ratio of ground velocity to pressure for a layered subsurface model. Such "pressure-loading" methods are not the only approach to modeling air-to-ground coupling; Tanimoto (2026) demonstrated that a normal mode formulation provides an equivalent representation to the forcing function approaches such as the propagator matrix.

In this study, we examine the seismic particle motion of AGCWs across a dense seismoacoustic network and at individual stations for air-to-ground coupled infrasound from the 2012 Camp Minden Explosion. We quantify the occurrence of prograde and retrograde motions and investigate their dependence on subsurface structure. We then model acoustic–seismic coupling using a propagator matrix technique for layered media, and then apply a Bayesian inversion framework to estimate shallow elastic parameters. By integrating observations and models, we aim to further our understanding of AGCWs and to support studies that leverage them to study both acoustic sources and subsurface properties.

2 Data

To explore air-to-ground coupling at a large scale, we examine seismoacoustic signals from the 2012 Camp Minden Explosion, recorded at stations with co-located acoustic and seismic instruments. At approximately 4:25:50 UTC on 16 October 2012, a munitions storage bunker (32.5694° N, 93.3525° W) containing demilitarized explosives detonated violently at Camp Minden Army Ammunition Plant in northwest Louisiana. The resulting blast shattered windows in a 6 km radius, derailed 11 nearby rail cars, and sent acoustic waves across the eastern United States (U.S. Department of Justice, 2018). Fortuitously, the EarthScope USArray Transportable Array (TA Meltzer et al., 1999) was deployed in an ideal position at the time of the explosion (Figure 1a). Wills et al. (2022) provides a comprehensive overview of seismoacoustic signals generated by the Camp Minden Explosion.

The EarthScope TA was a dense network of observatory-grade seismic stations that systematically migrated across the contiguous United States from 2004 to 2015. In 2014, the deployment began to move into Alaska and Western Canada, where it remained operational until 2021. The stations were initially equipped with only seismic instrumentation, and co-located microbarometers (infrasound sensors) were installed beginning in 2011. TA stations were equipped with broadband seismometers (Streckeisen STS-2, Güralp CMG-3T, and Nanometrics T-240) and Hyperion IFS-4532 infrasound sensors, both sampling at 40 Hz. This upgrade expanded the project's capabilities to study energetic acoustic events (de Groot-Hedlin and Hedlin, 2014; Sanderson et al., 2020).

Fortunately the TA was upgraded prior to the Camp Minden Explosion, making this event one of the most densely recorded anthropogenic explosions by a regional infrasound network. Of the 380 active TA stations in mid-October 2012, 240 recorded infrasound signals from the explosion, and 126 of those stations displayed clear acoustic–seismic coupled signals (Figure 1b,c). We use this dataset to examine the spatial distribution of coupled wave particle motion and to select stations for our subsequent inversion scheme.

3 Methods

3.1 Identification of air-to-ground coupling

To identify the frequencies at which strong acoustic–seismic coupling is occurring, we utilize the magnitude-squared coherence between the infrasound and vertical seismic channel ($C_{ZI}(\omega)$). Seismoacoustic coupling can sometimes be identified by simply examining seismic and acoustic waveforms. However, the magnitude-squared coherence provides a frequency-domain measure that identifies specific frequencies that have strong coupling (Matoza and Fee, 2014; Bishop et al., 2023). This is useful when examining particle motions, as we want to focus only on coherent frequencies to avoid capturing ambient seismic noise or non-coupled signals. The magnitude-squared coherence between the vertical seismic and infrasound is defined as

$$C_{ZI}(\omega) = \frac{|S_{ZI}(\omega)|^2}{S_{ZZ}(\omega)S_{II}(\omega)}, \tag{4}$$

where $S_{ZI}(\omega)$ is the cross-spectral density of the vertical seismic Z and infrasound signal I, and $S_{ZZ}(\omega)$ and $S_{II}(\omega)$ are the auto-spectra.

To identify and confirm strong air-to-ground coupling for Camp Minden seismoacoustic signals, we apply the magnitude-squared coherence in 10 s sliding windows with 90 % overlap, using Welch's method for spectral estimation with 2.5 s windows and 50 % overlap. We identify an AGCW detection by first defining time windows where we expect infrasound to arrive, using celerity values typical of infrasound propagation in tropospheric and stratospheric waveguides (≈280–340 m/s; (Whitaker and Mutschlecner, 2008; Fee and Matoza, 2013)). Within this time window, we inspect the seismoacoustic waveforms and coherence (C_{ZI}), and visually determine the presence of coupling. We first attempted an automated technique using acoustic–seismic coherence thresholds to identify an AGCW detection, however the presence of coherent noise introduced considerable false positive detections so we chose a manual method instead.

3.2 Quantifying seismic particle motion

Characterizing AGCW particle motion on numerous stations requires an efficient method. Traditional approaches often rely on waveform filtering and visual inspection of rotated horizontal and vertical seismograms (Langston, 2004; Berg et al., 2022), but these qualitative methods are impractical for analyzing hundreds of seismoacoustic stations across multiple frequency bands. To overcome this limitation, we employ a quantitative method called the Normalized Inner-Product (NIP). This approach, adapted from Meza-Fajardo et al. (2015), was developed to design filters to analyze seismic surface waves and has been used to identify Rayleigh waves in volcanic tremor (Hirose and Ueda, 2025). Here, we instead apply it in a time-frequency framework to quantify prograde and retrograde particle motion in seismoacoustic coupling.

First, for stations where coherent coupling is observed, three-component seismograms are rotated into radial-transverse coordinates based on the great-circle back-azimuth to a defined source location. This rotation implies two assumptions: (1) air-to-ground coupled infrasound excites motion only in the radial–vertical plane, and (2) the infrasound arrives at the station along the great-circle back-azimuth and is not affected by crosswinds. These assumptions are discussed later in the paper. Consider a harmonic representation of the vertical and radial displacements of a propagating seismic wave,

$$Z(\omega) = A_Z(\omega)e^{i\Phi_Z(t,\omega)}, \tag{5}$$

$$R(\omega) = A_R(\omega)e^{i\Phi_R(t,\omega)}, \tag{6}$$

where Φ_n is the phase angle for the nth component. We then apply a Hilbert transform (phase advance by $\frac{\pi}{2}$) to the vertical component (so that, for retrograde motion, the components are in-phase) to define:

$$\hat{Z}(\omega) = A_Z(\omega)e^{i\left(\Phi_Z(t,\omega)+\frac{\pi}{2}\right)}. \tag{7}$$

Next we compute the cross-spectrum of the shifted vertical and radial signals:

$$S_{\hat{Z}R}(\omega) = \hat{Z}(\omega)R^*(\omega). \tag{8}$$

where $*$ denotes the complex conjugate. The phase angle of the cross-spectrum represents the phase shift present in the frequency domain between vertical and radial components. We then normalize the cross-spectrum (Equation 9), so the values range from -1 to 1, where positive values indicate retrograde and negative values indicate prograde particle motion, which defines the NIP:

$$\mathrm{NIP}(\omega) = \cos\big(\arg(S_{\hat{Z}R}(\omega))\big). \tag{9}$$

To examine the geographic distribution of AGCW particle motion across TA stations, we determine the predominant sense of particle motion (prograde or retrograde) for a particular station by computing the median NIP value over time-frequency regions where $C_{ZI} > 0.7$. When classifying the number of stations that are predominantly prograde or retrograde, we require the median NIP to be below -0.5 for prograde, and to exceed 0.5 for retrograde, because an NIP near zero implies rectilinear motion.

We select a frequency band of 1.5–10 Hz for this analysis. The lower bound (1.5 Hz) corresponds to an approximate depth sensitivity of 34 m, assuming a pressure velocity (c) of 343 m/s and using the depth sensitivity relation ($h = 0.15\, c/f$) from Tanimoto and Wang (2019), where h is depth sensitivity and f is frequency in Hz. We note that this depth is an approximation for the depth of maximum sensitivity, not the maximum depth to which the waves are sensitive to. We chose this depth sensitivity so we could compare particle motions to V_{S30} estimates (Heath et al., 2020), which aim to characterize the shear-wave velocity of the upper 30 meters of the subsurface. The upper bound (10 Hz) is selected to preserve high-frequency information while minimizing contamination from noise at stations farther from the explosions, where high frequency energy is largely absent and signal–noise ratios are generally weaker. Although applying a coherence threshold should theoretically suppress such noise, some noise can remain coherent between both seismic and infrasound channels. For completeness, in the supplemental information we also analyze two additional bands: 1–6 Hz and 6–18 Hz.

To examine AGCW particle motion in a time-frequency analysis, we apply the NIP in a sliding window approach using 10 s windows with 90 % overlap. For the spectral estimation, we use Welch's method with 2.5 s windows and 50 % overlap. To aid in the isolation of coupling-specific ground motions, we mask time-frequency space by multiplying the NIP by the magnitude-squared coherence (Equation 4) between the infrasound and vertical seismic.

3.3 Modeling air-to-ground coupled waves

To model acoustic–seismic coupling in layered media, we employ a comprehensive framework to capture the complex particle motions observed in real data. We follow the approach of Xu and Lognonné (2024), who applied eigenfunction theory and a propagator matrix technique to solve for pressure-induced ground motions. Note that we use a different sign convention than Xu and Lognonné (2024), where we define the negative vertical component as downwards into the Earth. The subsurface is represented by n layers of finite thickness overlying a halfspace that extends to infinite depth. Below we provide a brief description of this method and refer the reader to Xu and Lognonné (2024) for more details.

First, we can define an eigenfunction vector describing particle motion and stress at depth z:

$$\vec{f}(\omega, z) = \begin{bmatrix} U_x \\ U_z \\ T_{zx} \\ T_{zz} \end{bmatrix}, \tag{10}$$

where U_x and U_z are the horizontal (or radial) and vertical displacement amplitudes and T_{zx} and T_{zz} are the shear and normal stresses. To solve for pressure-induced particle motions, we use two separate eigenfunction vectors for downgoing compressional waves:

$${}_P\vec{f} = \frac{\exp(-\gamma z)}{\omega} \begin{bmatrix} \alpha\omega/\hat{c} \\ \alpha\gamma \\ -2\alpha\mu\omega\gamma/\hat{c} \\ -\alpha\mu\left(\omega^2/\hat{c}^2 + v^2\right) \end{bmatrix}, \tag{11}$$

and shear waves:

$${}_S\vec{f} = \frac{\exp(-vz)}{\omega} \begin{bmatrix} \beta v \\ \beta\omega/\hat{c} \\ -\beta\mu\left(\omega^2/\hat{c}^2 + v^2\right) \\ -2\beta\mu\omega v/\hat{c} \end{bmatrix}, \tag{12}$$

where $\hat{c}$ is the apparent (trace) acoustic velocity; ω is the angular frequency; α and β are the compressional and shear-wave speeds; μ is the shear modulus; and $\gamma = \omega\sqrt{1/\hat{c}^2 - 1/\alpha^2}$ and $v = \omega\sqrt{1/\hat{c}^2 - 1/\beta^2}$.

The total wavefield at the surface must satisfy the zero shear-stress condition, and it can be described as a combination of compressional (P) and shear (S) waves:

$$\vec{f}(z_0) = {}_P\vec{f}(z_0) - \frac{{}_PT_{zx}(z_0)}{{}_ST_{zx}(z_0)}\,{}_S\vec{f}(z_0). \tag{13}$$

We can describe the horizontal and vertical compliance (ratio of ground velocity to pressure) using terms in the surface eigenfunction vector $\vec{f}(z_0)$:

$$C_z(z_0) = \frac{-i\omega U_z(z_0)}{-T_{zz}(z_0)}, \tag{14}$$

$$C_x(z_0) = \frac{-\omega U_x(z_0)}{-T_{zz}(z_0)}. \tag{15}$$

Therefore, the pressure-induced surface particle motions (those recorded by a seismometer) can potentially be recovered from $\vec{f}(z_0)$.

To solve for $\vec{f}(z_0)$, we employ a propagator matrix technique (Aki and Richards, 2002). Using the propagator matrix $\boldsymbol{P}$ (which is defined by the physical properties of a certain layer), we can solve for the eigenfunction vector at the surface beginning with the eigenfunction vector at the top of the halfspace ($\vec{f}(z_n)$):

$$\vec{f}(z_0) = \prod_{m=1}^{n} \boldsymbol{P}_m\left(z_{m-1} - z_m\right)\vec{f}(z_n). \tag{16}$$

Working our way up from the halfspace through n layers to the surface, we determine $\vec{f}(z_0)$. Using this method, we compute the compliance (C_z and C_x) for all frequencies (ω) of interest which serve as frequency-dependent vertical and horizontal transfer functions:

$$C_z(\omega) = \frac{-i\omega U_z(\omega)}{P(\omega)}, \tag{17}$$

$$C_x(\omega) = \frac{-\omega U_x(\omega)}{P(\omega)}, \tag{18}$$

where $P(\omega)$ is the Fourier amplitude of the pressure signal at ω.

To further interpret the physical nature of the coupled wavefield, we also examine the depth-dependent eigenfunctions for some models. These eigenfunctions describe how displacement and stress vary with depth for each frequency and can provide insight into both particle motion and wave propagation behavior. In particular, the relative signs of the vertical (U_z) and horizontal (U_x) displacement eigenfunctions at the surface can govern the sense of prograde or retrograde particle motion observed at the surface (Tanimoto and Rivera, 2005).

We construct a layered model to recreate AGCWs observed in this study. First, we choose a realistic apparent acoustic velocity $\hat{c}$. Each layer is defined by its compressional wave velocity, shear-wave velocity, density, thickness (except the underlying halfspace), and an optional quality factor (Q_μ). Q_μ incorporates shear wave attenuation into the model by modifying the shear modulus:

$$\mu^* = \mu \left(1 - \frac{i}{Q_\mu}\right). \tag{19}$$

The complex shear modulus μ^* can be used to define the propagator matrix $\boldsymbol{P}$ for different layers. Including Q_μ is optional because, as shown in Xu and Lognonné (2024), it is only required for air-coupled Rayleigh wave activation. This phenomenon occurs when the phase velocity of an incident acoustic wave matches the subsurface Rayleigh wave phase velocity, leading to efficient seismoacoustic energy transfer and quasi-monochromatic surface waves (Press and Ewing, 1951; Jardetzky and Press, 1952). Without Q_μ, synthetic air-coupled Rayleigh waves do not attenuate over time, though when these waves are not activated, Q_μ has little effect on the compliance (Xu and Lognonné, 2024).

After a compliance model is constructed, we must choose a pressure source to model ground motions using the transfer functions in Equations 17 and 18. Rather than using a synthetic source function, we use the recorded, colocated acoustic signal from stations where AGCWs of interest are observed. The acoustic data are processed with a zero-phase two-pole Butterworth filter with a passband that encompasses the frequencies with high vertical seismic-infrasound coherence ($C_{ZI}(\omega)$), corresponding to strong coupling.

3.4 Bayesian inversion for subsurface parameters

To constrain the subsurface properties that govern AGCWs, we invert the observed ground motion using the forward modeling framework (Section 3.3). We adopt a Bayesian approach and implement a Markov chain Monte Carlo (MCMC) method to sample from the posterior distribution of model parameters. This allows us to explore the space of realistic subsurface parameters.

For simplicity, our target subsurface model consists of a single layer over a halfspace. This structure is sufficient to capture frequency-dependent particle motions while keeping the parameter space small. We select the apparent acoustic velocity ($c = 348.3\,\mathrm{m/s}$) based on an incidence angle of 80° from the vertical (typical of stratospherically ducted infrasound; Fee and Matoza, 2013; Whitaker and Mutschlecner, 2008) and a sound speed of 343 m/s. The unknowns in the inversion for each layer are the shear-wave velocity, density, thickness (top layer), and a single quality factor applied to both media. Compressional-wave speeds are not treated as free parameters; instead, as a further simplification, we assume a Poisson solid so that the forward model computes α from a fixed α/β ratio of $\sqrt{3}$. We treat both the shear-wave velocity β and density as unknown parameters, as opposed to Tanimoto and Wang (2019), who found that seismoacoustic coupling of wind was relatively insensitive to density and solved only for the bulk modulus μ. While the coupling was mostly insensitive to density, it still has a non-zero effect. Therefore, we choose to include both β and density to retain the more intuitive value of shear-wave velocity, though we caution readers when interpreting the density results.

Prior distributions are specified as informed normal distributions centered on plausible values suggested by forward-modeling trials. In these trials, parameters were adjusted and the resulting waveforms and frequency-dependent particle motions were visually compared. Although not exhaustive, this process provided a reasonable starting point for the inversion. Observational noise levels are treated as additional unknown parameters with half-normal priors, allowing them to be inferred directly from the data and incorporated into the posterior distribution. The likelihood function compares the synthetic vertical and radial displacements generated by the forward model with the observed vertical and radial seismograms at each seismoacoustic station. For our inversions, we choose a slightly broader frequency band of 1–18 Hz to include additional coherent coupling present at lower frequencies.

We perform posterior sampling using the Metropolis-Hastings algorithm as implemented in PyMC (Salvatier et al., 2016), with six Markov chains. Each chain runs for 900,000 iterations, with the first half used for tuning and the second half retained as posterior draws. The computations for each station take approximately 10 hours using 6 CPU cores (one for each chain). Best-fit synthetic seismograms are produced by running the forward model with the median of the posterior parameter samples. Synthetic and observed waveform fits are evaluated using the normalized squared residual.

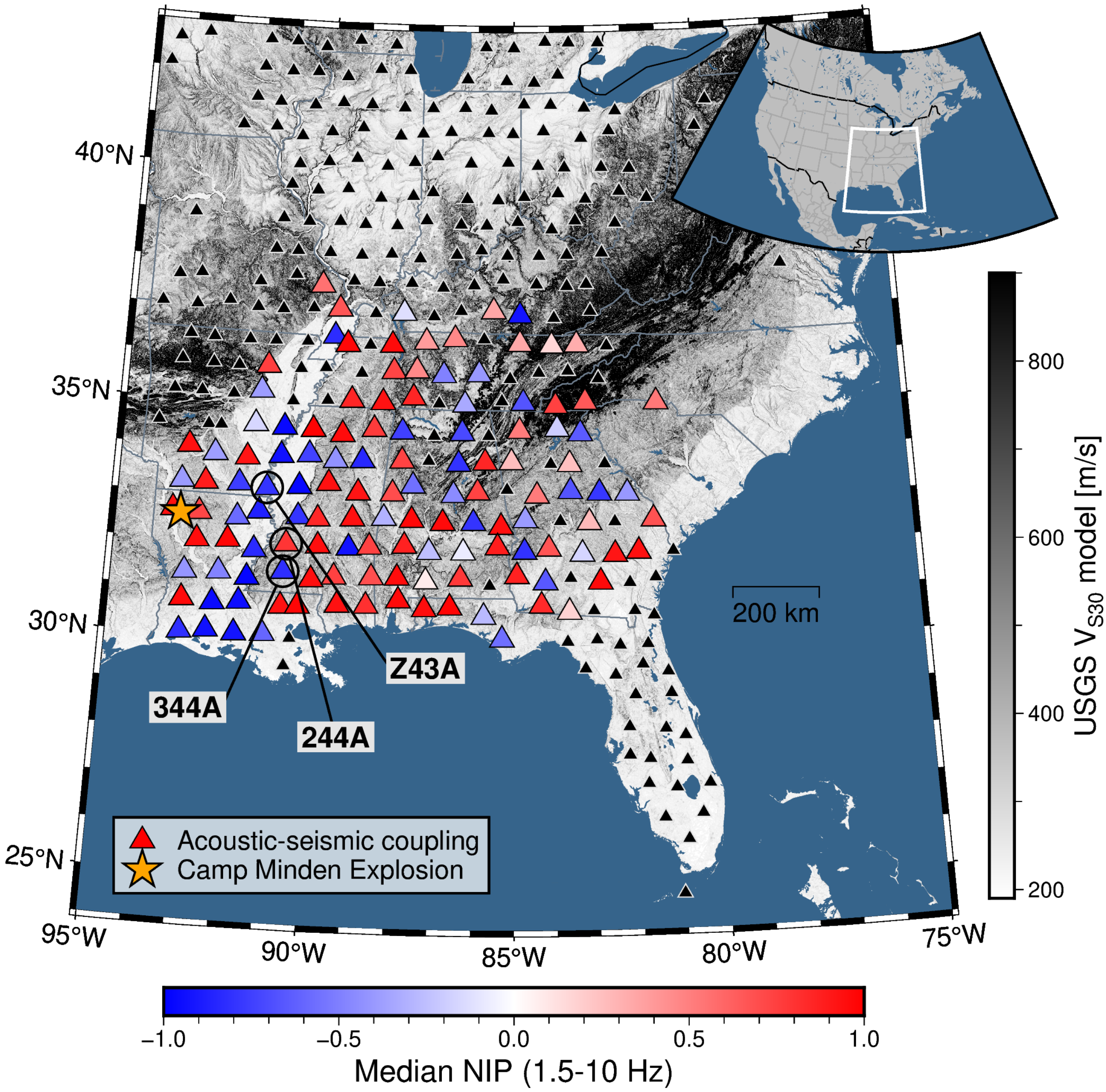

Figure 2 Spatial distribution of air-to-ground coupled wave particle motion from the 2012 Camp Minden Explosion, in the 1.5–10 Hz band. Blue triangles indicate stations with predominantly prograde particle motion and red triangles indicate retrograde. The basemap of this figure is the USGS V_{S30} model (Heath et al., 2020). The three stations we analyze further are labeled.

4 Results

4.1 Spatial variability of AGCW particle motions

For each TA seismoacoustic station that recorded AGCWs from Camp Minden, we examine the seismic particle motion using the NIP method. The spatial distribution of particle motion for the 1.5–10 Hz band is shown in Figure 2. While some scatter is present, clear patterns emerge in the spatial distribution of particle motion. There is a prevalence of prograde particle motion in the Mississippi Embayment. To the east of the Embayment, particle motion is predominantly retrograde (red triangles), though some stations intermittently exhibit prograde motion or no overall sense of motion (white). In total, 60 stations exhibit predominately retrograde motion and 35 are predominantly prograde. Comparing the observed particle motions with the USGS V_{S30} model (grayscale basemap), we find that many prograde stations coincide with areas of particularly low V_{S30}, whereas retrograde stations are more common in regions of higher shear-wave velocity. This relationship, however, is not systematic: prograde motion also occurs in areas of high V_{S30}, and retrograde motion in low-V_{S30} regions.

We also examine two additional frequency bands (1–6 Hz and 6–18 Hz), whose results are shown in Supplemental Figure S1. In the 1–6 Hz band (Figure S1a), we determine 58 stations have predominantly retrograde particle motion, and 35 have predominantly prograde motion. This is essentially the same as in the 1.5–10 Hz band. In the 6–18 Hz band (Figure S1b), we identify 56 stations with predominantly retrograde particle motion and 43 with predominantly prograde motion. In

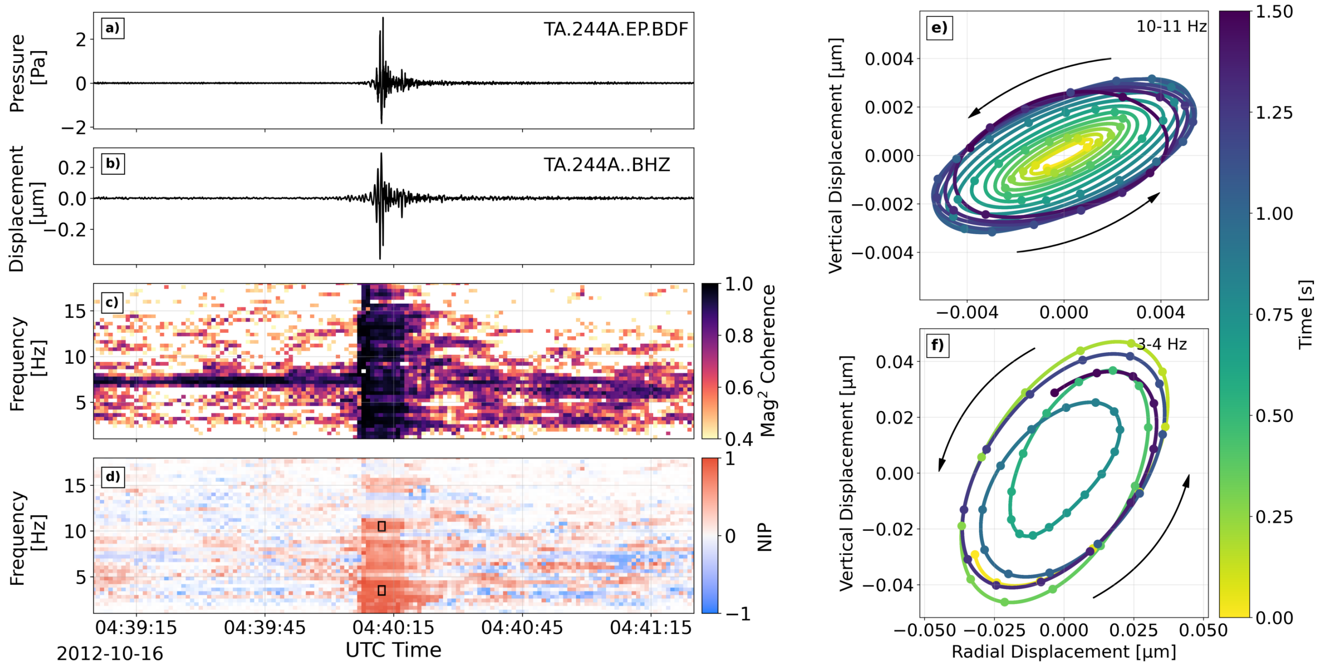

Figure 3 Air-to-ground coupling at station TA.244A. **a)** Infrasound waveform and **b)** vertical seismic waveform, both filtered 1–18 Hz. **c)** Magnitude-squared coherence between pressure and vertical seismic. Darker colors indicate strong coupling. **d)** Time-frequency Normalized Inner Product (NIP) using rotated seismograms. Red indicates retrograde particle motion, blue indicates prograde. The transparency of the values is determined by $(C_{ZI})^2$, to highlight the strongest seismoacoustic coupling. The black rectangles indicate time-frequency space for particle motion analysis shown in the right column. **e)** Radial–vertical particle motions for the 10–11 Hz band. Dots indicate observed data points and lines connecting are interpolated. **f)** Radial–vertical particle motions for the 3–4 Hz band.

this higher band, the relative number of prograde stations increases and the number of retrograde stations decreases slightly. However, the shift from retrograde to prograde motion is not absolute when moving from lower to higher frequencies. Looking closely, there are several stations where the particle motions switch from prograde at lower frequencies to retrograde at high frequencies. Supplemental Figure S1c shows the difference in NIP value between the higher frequency (6–18 Hz) and low frequency (1–6 Hz) results, which shows how the character of frequency-dependent particle motions vary significantly. We also compare the median station NIP to V_{S30} in these two bands in Supplemental Figure S2.

The spatial patterns in particle motion observed in this study (focusing on 1.5–10 Hz) are similar to the findings of Wills et al. (2022), who calculated coupling coefficients (the ratio of ground velocity to pressure, analogous to compliance) and seismoacoustic coherence for the same signals we analyze. They found that acoustic–seismic energy transmission was greatest in flat-lying regions (often used as a proxy for low V_{S30}) such as the Mississippi Embayment and weakest in mountainous areas such as the Appalachian Mountains. Seismoacoustic coherence exhibited a similar pattern, with the highest coherence occurring where energy transmission was lowest. Our results show a comparable spatial pattern, with prograde motion in regions of low coherence and high energy admittance identified by Wills et al. (2022), though the trends in our data are less pronounced and exhibit greater variability. It is important to note that our analysis examines a different frequency band than Wills et al. (2022), who focused on the 2–4 Hz range.

4.2 Station-specific AGCW particle motions

While the preceding section emphasizes spatial trends in AGCW particle motion, here we analyze the frequency-dependent behavior at individual stations. We present observations of air-to-ground coupling at three stations with distinctly different coupling characteristics. First, we examine station TA.244A, positioned in western Mississippi (32.0421°, -90.6856°) but geographically outside the Mississippi Embayment (Figure 2). 244A is approximately 258 km from Camp Minden at an azimuth of 102.4°. Infrasound and seismic waveforms, seismoacoustic coherence, and particle motion can be seen for this station in Figure 3. At 244A, we observe high signal–noise infrasound and vertical seismic amplitudes, with broadband, coherent coupling in the 1–18 Hz band. Looking at the particle motions (Figure 3d), retrograde motion clearly dominates the entirety of the frequency band. We determine the transparency of time-frequency NIP values in Figure 3d with $(C_{ZI})^2$, to highlight the strongest seismoacoustic coupling. We also examine the radial–vertical displacements in two bands with NIP values near 1 (Figure 3e,f), and confirm that retrograde motion dominates, though the distribution of radial and vertical amplitudes differ. In the 3–4 Hz band, vertical amplitudes dominate, whereas the 10–11 Hz

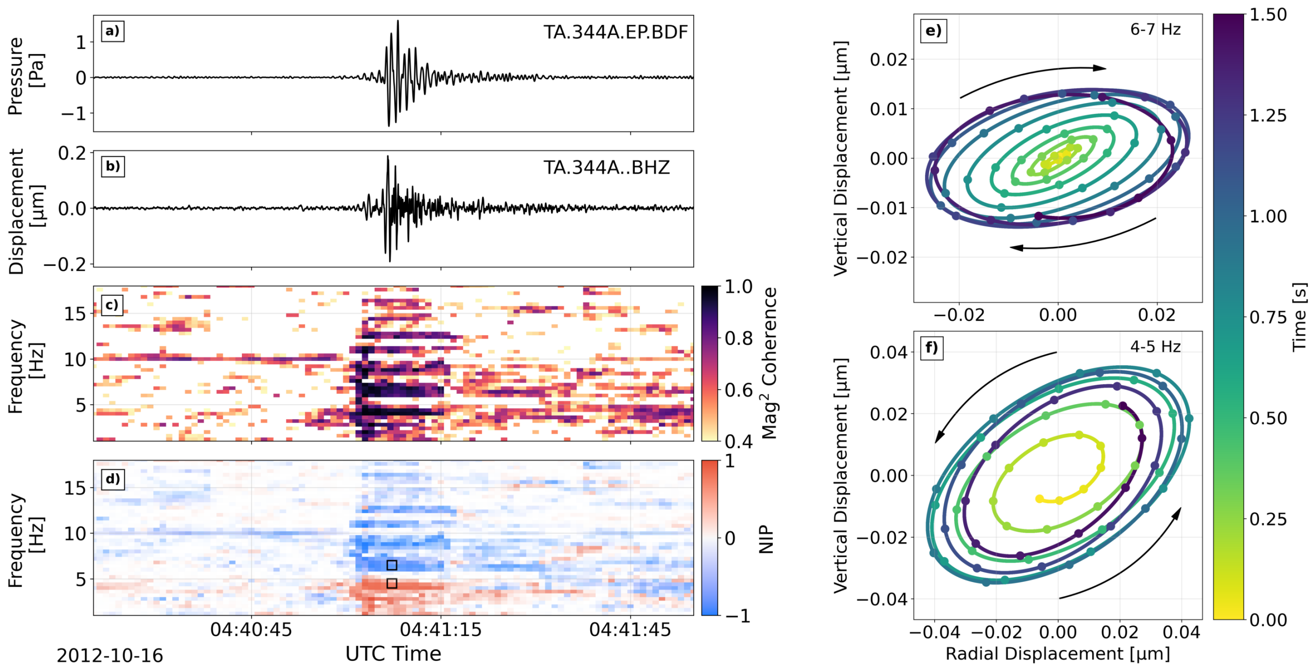

Figure 4 Air-to-ground coupling at station TA.344A. Panels contents are the same as Figure 3. Infrasound and seismic waveforms are similarly filtered 1–18 Hz. Frequency-dependent particle motion is clearly observed in panels **d)**, **e)** and **f)**.

band show more radial motion.

Interestingly, despite strong coherence in frequencies above 12 Hz the particle motion becomes less clear and some time-frequency bins display an NIP of $\simeq 0$, which indicates that the radial and vertical displacements are in-phase. Preceding the infrasound signal, some monochromatic coherence is observed at ~7 Hz (Figure 3c), however the abrupt onset of retrograde particle motions upon the arrival of the infrasound signal reveals that this noise likely does not contaminate our analysis.

Next, we analyze particle motions at TA.344A, located in southwest Mississippi (31.4527°, -90.7317°), which is also geographically outside of the Mississippi Embayment. 344A is approximately 277 km from Camp Minden at an azimuth of 115.9°. Air-to-ground coupling at TA.344A is shown in Figure 4, where the coupling pattern is notably complex. Unlike TA.244A (Figure 3), 344A does not exhibit broadband infrasound-seismic coherence. Instead, the coherence appears banded, with prominent coherent frequencies interspersed by incoherent gaps. The particle motions are equally intriguing: retrograde motion dominates up to approximately 5 Hz before transitioning to prograde motion.

We examine radial–vertical seismic displacements for station 344A within two of these coherent bands (Figure 4d-f). The frequency bands we select are 4–5 Hz and 6–7 Hz, representing two opposing senses of particle motion. As seen in Figure 4e-f, the lower-frequency band exhibits clear retrograde motion, with radial and vertical displacements of roughly equal amplitude. In contrast, the higher frequency band is dominated by radial displacement and exhibits prograde motion.

The final station we analyze is TA.Z43A, located in southeast Arkansas (33.2100°, -91.2441°) within the Mississippi Embayment, approximately 11.5 km southwest of the Mississippi River. Z43A is approximately 210 km from Camp Minden at an azimuth of 69.6°. As shown in Figure 5 and 2, this station exhibits predominantly prograde particle motion. A notable feature of the coupling for this station is observed in the vertical seismic displacement (Figure 5b), which shows a high-amplitude monochromatic wavetrain lasting several seconds before decaying to background noise. The onset of this monochromatic signal coincides with the largest pressure pulse but persists well beyond the duration of significant infrasound energy in Figure 5a, likely indicating the activation of a surface wave. Similar to 244A, the seismoacoustic coherence here shows prominent frequency-dependence, with some notable gaps and frequencies with particularly strong coupling.

The radial–vertical displacements for a 1.5 s time window are shown in Figure 5e,f. As observed at station 244A (Figure 3), there is no frequency-dependent change between prograde and retrograde motion; however, the amplitude distributions differ significantly (also note the large difference in axes scale). The low-frequency band (1–2 Hz) exhibits motion that is predominantly vertical, whereas the higher-frequency band (9–11 Hz) shows a greater radial component.

4.3 Bayesian inversion for subsurface velocity structure

In an effort to constrain the shallow subsurface properties that govern these complex particle motions, we applied a Bayesian inversion scheme in conjunction with our propagator-matrix forward modeling approach. In this framework, we estimate shear-wave velocity, density, and thickness for a simplified subsurface consisting of a single layer over a halfspace.

Inversion results for station 244A (Figure 2) provide

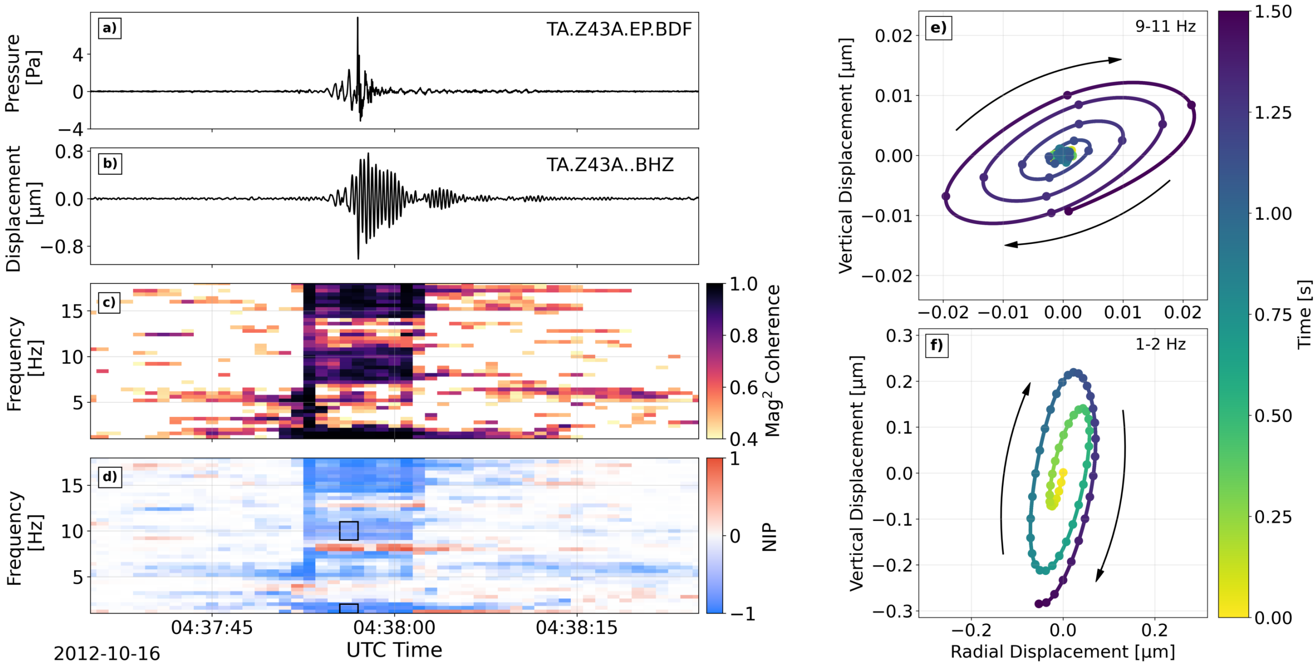

Figure 5 Air-to-ground coupling at station TA.Z43A. Panels contents are the same as Figures 3 and 4. Infrasound and seismic waveforms are filtered 1–18 Hz. We observe broadband prograde motion, though some frequencies lack a definitive particle motion.

a good fit to the data. Synthetic seismograms generated with the best-fitting inversion parameters, along with probability density functions (PDFs) of the posterior samples, are shown for station TA.244A in Figure 6. The median posterior model consists of a 67 m thick upper layer with a shear-wave velocity of 418 m/s and a density of 1716 kg/m^3, underlain by a halfspace with a shear-wave velocity of 556 m/s and a density of 1907 kg/m^3. Notably, no quality factor Q_μ is required for this example. Running the inversion both with and without Q_μ produces nearly indistinguishable synthetic waveforms and parameter estimates (Supplemental Figure S3), suggesting that air-coupled Rayleigh wave activation did not occur.

Posterior distributions for each layer are roughly Gaussian. Some parameters show greater standard deviations, while others like the top layer shear-wave velocity are tightly constrained, which may suggest lower parameter uncertainty or consistency with our assumptions. The synthetic waveforms produced by this model closely match the observations. The normalized squared residual (NSR) between the modeled and observed vertical and radial displacements are 0.19 and 0.56, respectively. The fit is superior for the vertical channel, though the observed horizontal has a lower signal–noise ratio, and the presence of noise unrelated to coupling could explain larger discrepancies in the observed and modeled waveforms.

At TA.344A (Figure 2), the inversion is markedly less successful than at 244A, as seen in Figure 7. While the inversion produces Gaussian PDFs of posterior samples, we believe these values cannot be trusted and are likely artifacts of the priors. The median posterior parameters are made up of a 11 m thick upper layer with a shear-wave velocity of 468 m/s and a density of 1462 kg/m^3, overlying a halfspace with a shear-wave velocity of 1170 m/s and a density of 1874 kg/m^3. The median Q_μ is 0.3. We include Q_μ because its presence would be necessary if an air-coupled Rayleigh wave is excited, but if not, it has little impact on the results (Xu and Lognonné, 2024).

As seen in Figure 7b-c, the modeled seismograms do not fit the observed data well at station 344A. A notable feature of the waveforms is uncaptured by the model: the vertical seismic component shows a pronounced low-frequency oscillation that mirrors the infrasound waveform, while the radial component instead displays a distinct high-frequency signal. We test numerous variations of the inversion (adjusting priors, changing the number of draws and tuning iterations, and modifying the filter for the input infrasound), but none of these attempts yield an improved fit to the observations.

The last station we present inversion results for is TA.Z43A (Figures 2,8), and the inversion produces good fits to the data with reasonable subsurface parameters. The character of seismoacoustic signals at this station is interesting. The infrasound is somewhat impulsive and broadband, the vertical seismic component is largely monochromatic, and the radial seismic notably lacks this ≈3.2 Hz monochromatic signal. It instead shows a low-frequency oscillation coincident with the impulsive infrasound. Similar to the other results, posterior PDFs for parameters are Gaussian, but with a varied degree of spread. For Z43A the halfspace shear-wave velocity has a particularly tight distribution. The median posterior model indicates a 32 m thick upper layer with a subsonic shear-wave velocity of 228 m/s and a density of 1751 kg/m^3, underlain by a halfspace with a shear-wave velocity of 348 m/s and a density of 2824 kg/m^3. There is no quality factor Q_μ in the posterior parameters. This

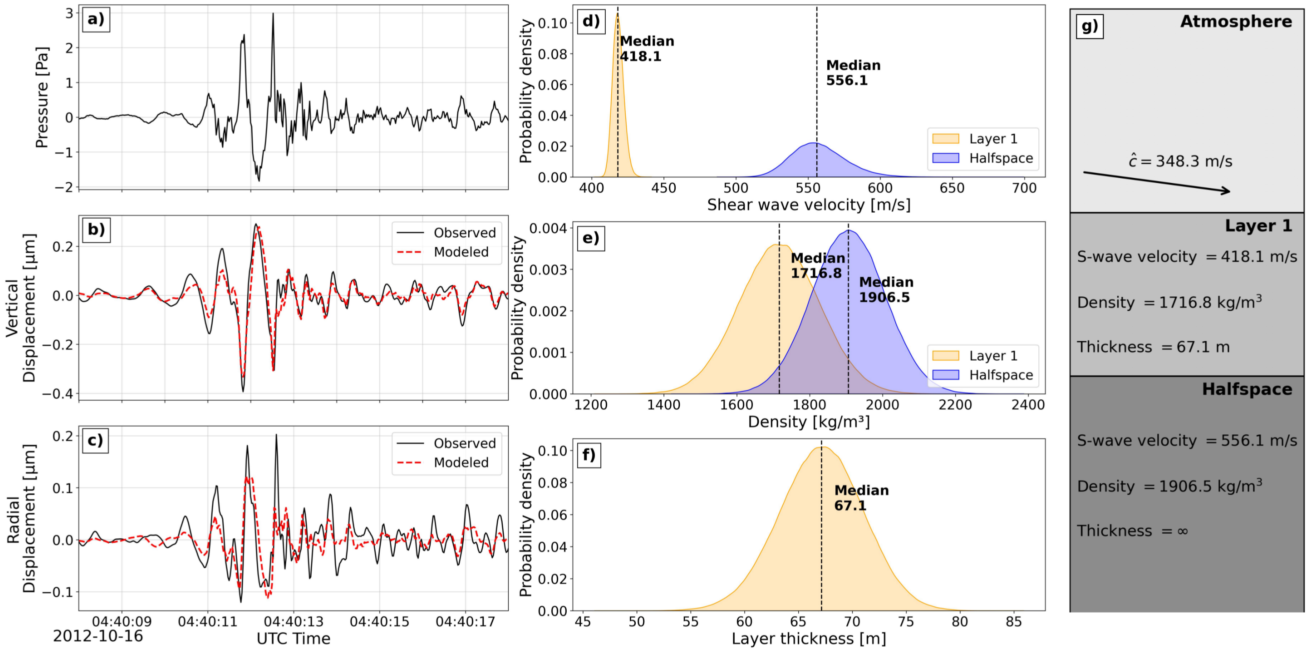

Figure 6 Inversion results at station TA.244A for subsurface properties. **a)** Infrasound waveform filtered between 1–18 Hz and **b)** modeled (red) and observed (black) vertical and **c)** radial seismic waveform. **d-f)** Probability density functions of samples from the posterior distribution for various subsurface model parameters. **g)** Diagram of the best-fitting subsurface model.

choice is made because, similar to 244A, the best-fitting parameters remain virtually the same whether we include it or not (Supplemental Figure S4). A detailed interpretation of why we can omit Q_μ is found in section 5.2 in the Discussion.

The best-fitting synthetic seismograms for station Z43A (Figure 8, left column) reproduce the vertical displacement remarkably well (NSR = 0.14), while the radial fit is fair but shows discrepancies (NSR = 1.30). Similar to TA.344A, the signal–noise ratio is substantially higher on the vertical component compared to the radial component, which may contribute to the difference in fit. Another notable observation is the absence of monochromatic waves on the radial component in both synthetic and observed seismograms, contrasting with typical Rayleigh-wave behavior, where such oscillations typically appear on both components.

5 Discussion

5.1 Spatially variable and frequency-dependent AGCW particle motion

The sense of AGCW particle motion (prograde or retrograde) during the 2012 Camp Minden explosion shows a clear spatial pattern across the Transportable Array (Figure 2). Prograde motion predominates in areas with low shallow shear-wave speeds (V_{S30}), particularly within the Mississippi Embayment, whereas retrograde motion is more frequent in higher-velocity areas. These observations support the theory in Bishop et al. (2022) and observations of Langston (2004) that prograde motion occurs when the apparent acoustic velocity exceeds the subsurface shear-wave velocity. The distribution of particle motion is also highly similar to the findings of Wills et al. (2022), who demonstrated that acoustic–seismic energy transfer was particularly efficient in flat-lying areas like the Mississippi Embayment.

While there is a general correlation between low V_{S30} and prograde particle motion, this relationship is not absolute (see Supplemental Figure S2). Several stations in eastern Georgia (approx. 32°, -82°; on the Atlantic Coastal Plain) exhibit clear retrograde motion despite very low V_{S30}, and a few stations in northern Alabama (approx. 34°, -87°) show prograde motion despite relatively higher shear-wave speeds (Figure 2). We ascribe these exceptions primarily to assumptions in the NIP method and the uncertainty inherent to the V_{S30} model, which is derived from topographic slope rather than direct measurements. While topographic slope provides a useful first-order estimate of seismic velocities (Wald and Allen, 2007), shallow subsurface geology (and therefore V_{S30}) can vary significantly over short distances (Zhou et al., 2023; Savran and Olsen, 2016). Using air-to-ground coupled infrasound from the Hunga, Tonga eruption, Macpherson et al. (2025) estimated shallow (≈35 m depth) shear-wave velocity and found discrepancies when comparing to the USGS V_{S30} model. In the context of the uncertainties in the USGS V_{S30} model, AGCW particle motion may offer a complementary or perhaps more direct indicator of low shallow shear-wave velocity. If a successful indicator, this could make AGCW a valuable tool in the field of seismic hazard assessment and site characterization (Castellaro et al., 2008).

We must also consider the potential influence of acoustic incidence angle on the dominant particle motions observed. The transition between retrograde and

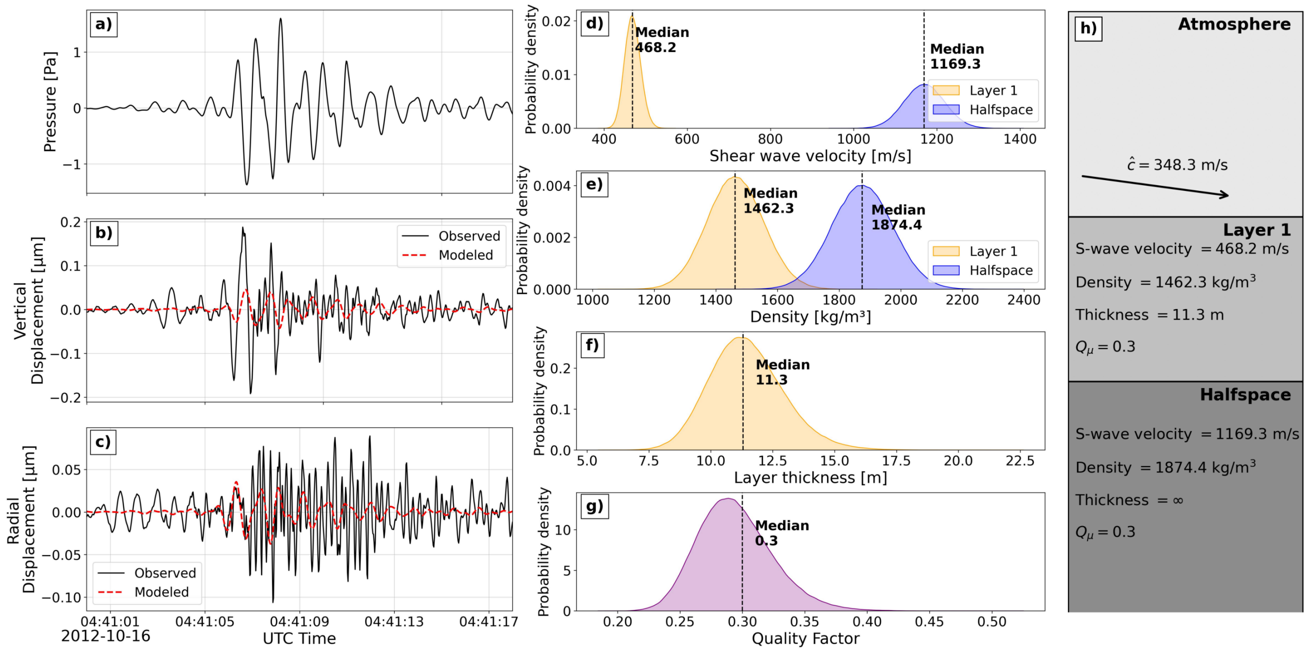

Figure 7 Inversion results at station TA.344A for subsurface properties. Input Infrasound waveforms are filtered 1–18 Hz. Panel contents are the same as Figure 6, except the inclusion of Q_μ in the posterior distributions. Best-fitting synthetic waveforms in panels **b-c)** show a poor fit with the observed data.

prograde depends on both the apparent acoustic velocity and the subsurface velocity (Bishop et al., 2022), therefore variations in the incidence angle of the arriving infrasound wavefront could influence the observed sense of particle motion. Wills et al. (2022) performed infrasound propagation modeling for the 2012 Camp Minden Explosion and found that infrasound propagated towards TA stations in a strong easterly stratospheric jet and a weaker tropospheric jet to the southeast. If incidence angle variations associated with these two atmospheric waveguides strongly controlled the observed particle motions, one might expect a spatial pattern consistent with the predicted distribution of acoustic energy. However, we find no clear correlation between the expected regions with stratospheric or tropospheric energy and dominant particle motions. This suggests that variations in apparent acoustic velocity caused by propagation are likely a secondary influence on particle motion relative to variations in subsurface velocity structure.

Some stations in Figure 2 show a median NIP of ∼ zero, indicating no predominant sense of particle motion. We attribute this to the frequency dependence of particle motion, as observed at TA.344A (Figure 4). When a transition between prograde and retrograde motion occurs within the 1.5–10 Hz band, the contributions from different frequencies can effectively "cancel out," resulting in a near-zero median NIP across the band. Many stations exhibit this frequency dependence, as illustrated in Supplemental Figure S1c, which shows the difference in NIP between the 1–6 Hz and 6–18 Hz bands. These changes in particle motion are likely attributed to subsurface structure and are discussed more in the following paragraphs.

While frequency-dependent transitions in particle motion can explain some variability in the NIP results, additional assumptions inherent to the NIP method could also introduce inaccuracies. In our analysis, seismograms are rotated into radial and transverse components using the great-circle back-azimuth to the source. However, this direction may not coincide with the true arrival direction of the acoustic wavefront. Atmospheric cross-winds can advect infrasound, producing deviations between the actual arrival direction and the assumed great-circle path (Vergoz et al., 2022; Blom et al., 2014). At the source-receiver ranges examined here (e.g., $<$1500 km), we expect this to be less than 5 degrees (Nippress and Green, 2023), and likely not significant. Furthermore, the NIP calculation assumes that acoustic energy transfers only into the vertical and radial components, yet observations have shown evidence of considerable coupling in the transverse component (Macpherson et al., 2025; Wills et al., 2022). Additionally, McPherson et al. (2026) performed 3D spectral-element modeling of acoustic–seismic coupling in complex topography and found that considerable AGCW energy was present on the transverse component in these scenarios. We propose this effect could result from coupling into a sloped surface plane that is rotated away from the angle normal to the incoming wavefront, causing the coupling to appear transverse when seismograms are rotated to the direction of the acoustic wavefront. These deviations from the ideal assumptions, if significant in our data, could lead to biased or inaccurate estimates of particle motion derived from the NIP methodology.

These methodological effects aside, the observed frequency-dependent transitions in particle motion are physically meaningful. If prograde motion arises from low shear-wave velocity, then a shallow unconsolidated

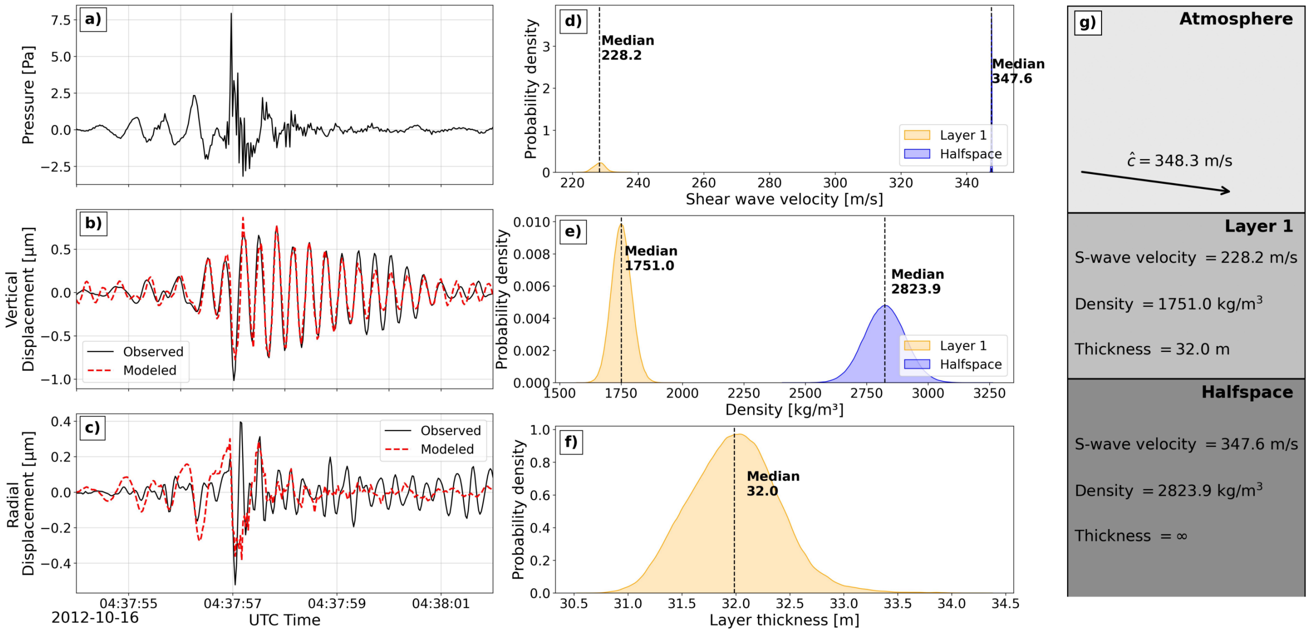

Figure 8 Inversion results at station TA.Z43A for subsurface properties. Input Infrasound waveforms are filtered 1–18 Hz. Panel contents are the same as Figure 6. The monochromatic signal in the vertical seismic waveform is reproduced very well by the best-fitting subsurface model, while the radial fit is reproduced moderately well.

low-velocity layer overlying more compact sediments or bedrock could produce the transition observed at 344A (Figure 4). The high frequency components of AGCWs are sensitive to very shallow depths, whereas lower frequencies probe deeper into the subsurface, leading to shifts in particle motion as the effective sampling depth changes. Satellite imagery reveals that Station 344A is located within the floodplain of McGeehee Creek, which provides a plausible example of this mechanism: unconsolidated low-velocity stream sediments overlying more competent material could produce the observed transition in particle motion (Figure 4). To validate our interpretation, we searched for well logs, active-source seismic surveys, and other near-ground-truth information, but no data close enough to the station (or any stations examined in this study) are available for comparison. While we observe more transitions from low-frequency retrograde to high-frequency prograde motion, the reverse scenario also occurs frequently (Figure S1c). This behavior can likewise be explained by subsurface structure, for example if a low-velocity layer lies under more competent material.

We also note that there are likely other mechanisms for prograde particle motion than very low subsurface shear-wave speeds. For example, we have observed prograde AGCWs at low frequencies (0.01–0.15 Hz) at AK.R16K (Supplemental Figure S5) and AK.A21K in Alaska from air-to-ground coupled infrasound sourced from the eruption of Hunga volcano, Tonga (Macpherson et al., 2025). At the depths that these AGCW frequencies are sensitive to (nearly 5 kilometers) it is physically implausible that the shear-wave velocity is sub-acoustic, so alternative mechanisms must exist for prograde motion. Unless this particular observation is the result of a sensor issue, perhaps it could be caused by a rapid change from high to low velocity with depth.

5.2 Physical interpretation of inversion results

We now interpret the inferred subsurface models and examine the composition of the air-to-ground coupled seismic wavefield at stations TA.244A and TA.Z43A. Due to little confidence in the results at TA.344A (Figure 7), we omit interpretations for that site and will discuss possible reasons for the inversion's failure in the following section.

Station 244A displays broadband retrograde particle motion and coupled seismic waveforms that are highly similar to the incident acoustic waveform (Figure 3). The best-fitting subsurface model from the inversion consists of a thick upper layer with a shear velocity exceeding the apparent acoustic velocity, overlying a halfspace with still higher velocity and density. This configuration is physically plausible, showing increasing velocity with depth and values consistent with typical near-surface materials like soil (Anbazhagan et al., 2016).

The case of coupling we observe at 244A is indicative of static loading. Here the velocity contrast between the atmosphere and Earth is great enough that a near-horizontally propagating acoustic wave arrives in excess of the critical angle, so compressional and shear waves are not directly transmitted. Instead, an evanescent wave (also called an inhomogeneous wave) is transferred, which decays rapidly with depth (Tanimoto, 2024; Xu and Lognonné, 2024). This case of coupling leads to the retrograde elliptical particle motions (Figure 3f) described in Ben-Menahem and Singh (1981), and serves as an excellent example of what is described in this theory.

In contrast to 244A, Z43A shows broadband prograde motion and waveforms indicative of a complex coupling scenario (Figure 5). The subsurface model here (Figure 8) has a top layer with a sub-acoustic shear-wave velocity (228 m/s), and a halfspace with a shear velocity that is slightly less than the apparent acoustic velocity. Notably, the inferred shear velocity (β) of the upper layer satisfies the condition proposed by Bishop et al. (2022) for prograde motion in a homogeneous half-space ($\hat{c} > \sqrt{2}\beta$). While most parameters in the model are physically plausible, the halfspace density (≈2824 kg/m^3) should be treated with caution. This value, while typical for continental crust (Christensen and Mooney, 1995), is very high for a depositional setting like the Mississippi Embayment and paired with such a low shear-wave velocity it is physically unrealistic. We pose that the inversion could be less sensitive to the density of the halfspace because at the lowest frequency we examine (1 Hz), the depth sensitivity is ≈50 meters, which primarily encompasses the upper layer (32 m thick). The apparent low sensitivity to density, particularly with increasing depth, parallels the findings of Tanimoto and Wang (2019).

Examination of the vertical seismic waveform at Z43A (Figure 8) indicates activation of a surface wave. At first glance, one may categorize this as an air-coupled Rayleigh wave (ACRW). However, recall the lack of a need for Q_μ in the inversion, suggesting that the apparent ACRW does not need to be dampened by attenuation in our forward model. Instead, we believe these observations are consistent with a leaky-mode surface wave (Xu and Lognonné, 2024; Aki and Richards, 2002). Here, the surface wave amplitude decays over time due to SV wave leakage into the halfspace, so Q_μ is not necessary. This interpretation is also consistent with the condition for leaky waves described in Xu and Lognonné (2024), where the apparent velocity is less than the compressional wave velocity of the halfspace but greater than the halfspace shear-wave velocity ($\beta_2 < \hat{c} < \alpha_2$). To further support this interpretation, we compute Rayleigh wave phase velocities using *pysurf96* (Herrmann, 2013) for the best-fitting subsurface model in Figure S4 (which includes Q_μ). We find that the apparent acoustic velocity (348.3 m/s) does not match the Rayleigh wave phase velocity when the ≈3.2 Hz activation occurs (≈250 m/s; Supplemental Figure S6).

Examining how displacement eigenfunctions vary with depth and frequency provides a valuable perspective for interpreting acoustic–seismic coupling phenomena. To illustrate this, we examine the real part of the depth-dependent displacement eigenfunctions for the best-fitting layered model for Z43A from Figure 8, focusing on a frequency above (5 Hz) and below (2 Hz) the ≈3.2 Hz seismic energy activation. Supplemental Figure S7 shows the real part of the vertical (U_z) and horizontal (U_x) displacement eigenfunctions from the surface to 80 m depth. Of particular interest is the value of the eigenfunctions at the surface: at 2 Hz, both vertical and horizontal eigenfunctions are positive, whereas at 5 Hz the horizontal eigenfunction is negative. Following Tanimoto and Rivera (2005), the sign of the surface ratio U_z/U_x governs the sense of particle motion, where a positive ratio indicates prograde and a negative ratio is retrograde. For Rayleigh waves, Tanimoto and Rivera (2005) showed that the transition between prograde and retrograde motion is primarily controlled by changes in the sign of the vertical eigenfunction at the surface. Interestingly, for air–ground coupled waves we find that the sense of particle motion is instead controlled by the sign of the horizontal surface eigenfunction.

While a leaky-mode surface wave solution is favored for the inversion at Z43A, it is possible that an alternate solution with an air-coupled Rayleigh wave is also possible. In Supplemental Figure S4, some posterior samples are explored that correspond to models with a higher upper-layer velocity and a lower halfspace velocity. Combined with the inclusion of Q_μ, this alternative configuration may potentially represent a scenario in which an ACRW fits the observed data.

A key assumption in our inversion framework is the use of a single apparent acoustic velocity (348.3 m/s). In reality, this velocity carries appreciable uncertainty that could plausibly be on the order of several to ∼10 m/s. Because air-to-ground coupling depends strongly on this parameter's relationship with the subsurface seismic velocities, this assumption likely influences the best-fitting model parameters in our inversion. In particular, the excitation of surface waves (and the frequency at which they occur) depends on whether the apparent acoustic velocity matches the Rayleigh wave or leaky-mode wave phase velocity in the subsurface. As a result, parameters that strongly influence the dispersion characteristics of the subsurface model, such as the halfspace shear-wave velocity (Figure 8d), may shift if a different apparent velocity were assumed. While the inversion results produce useful constraints on the range of plausible subsurface structures, the best-fitting parameters should be interpreted with this uncertainty in mind. Future studies could reduce this uncertainty by using co-located infrasound arrays at seismoacoustic stations to better constrain the apparent acoustic velocity.

5.3 Limitations of the AGCW subsurface inversion

While our inversion scheme successfully reproduces AGCWs at several selected stations, limitations remain even in the apparently successful cases. Figure 9 compares the subsurface compliance model and the frequency content over time for the modeled and observed vertical seismic waveforms at Z43A. For the compliance model shown in Figure 9a, both real (solid line) and imaginary (dashed line) parts are present, corresponding to the active and reactive parts of the compliance, respectively (Godin, 2021). The non-negative real (active) component represents energy removed from the seismic wavefield through SV wave leakage into the halfspace, producing intrinsic attenuation even in the absence of the quality factor Q_μ. The imaginary (reactive) component reflects the storage and release of elastic energy, analogous to the behavior observed during static loading (Xu and Lognonné, 2024).

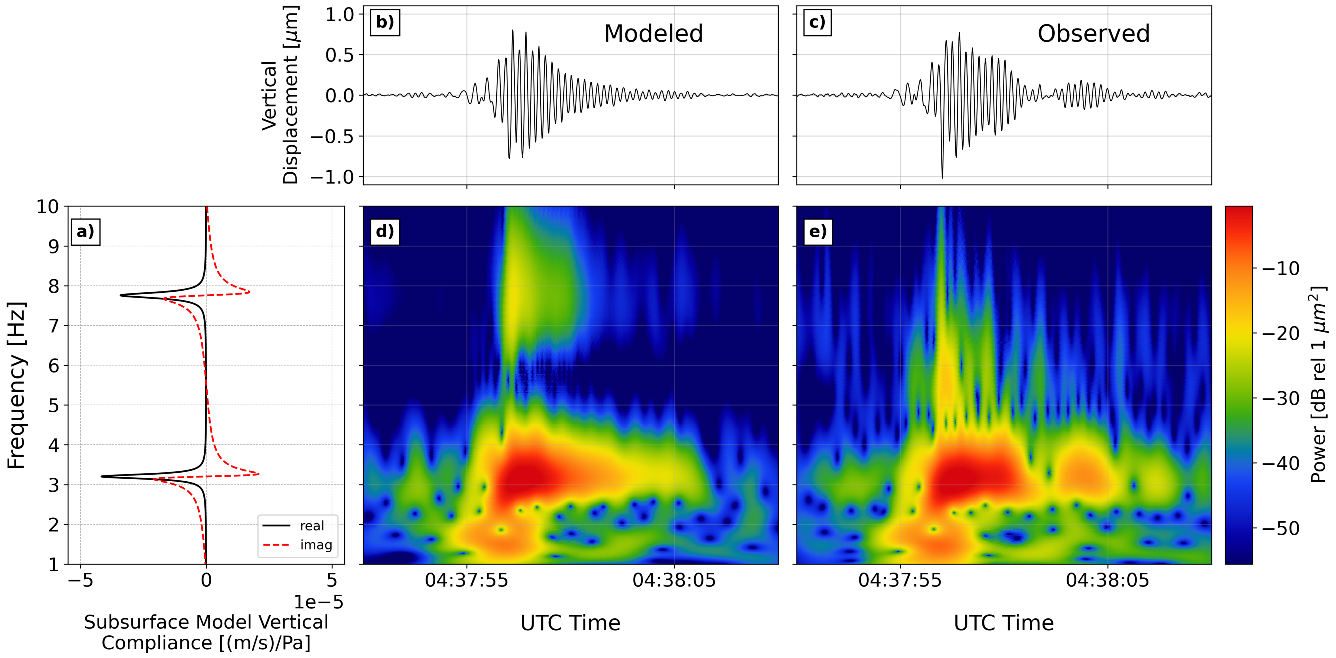

Figure 9 Comparison of modeled and observed air-to-ground coupling at station Z43A. **a)** Vertical compliance as a function of frequency for the best-fitting subsurface model parameters seen in Figure 8. Black and red lines denote the real and imaginary components, respectively. **b)** Modeled vertical seismic waveform. **c)** Observed vertical seismic waveform **d)** Continuous wavelet transform (CWT) scalogram of the modeled seismic waveform. **e)** CWT scalogram of the observed vertical seismic waveform.

Examining the spectral content of the observed signal (Figure 9e) is essentially a way to view the observed compliance, and is useful to compare with the modeled compliance (Figure 9a). The low-frequency spectral content around 3.2 Hz is reproduced exceptionally well; however, the model compliance also predicts a high-frequency "activation" near 8 Hz (Figure 9a,d) that is absent in the observed data (Figure 9e). Some higher-frequency content is present in the observations around 5–6 Hz, but it does not match that of the model.

This discrepancy in Figure 9 likely arises because in our Bayesian framework the likelihood is evaluated based on the filtered waveforms. This means if one frequency dominates the amplitudes, it will effectively suppress contributions from lower-amplitude frequencies. For Z43A, this reduces the inversion's sensitivity to the higher-frequency portions of the waveform. We attempted to address this by evaluating the likelihood using observed compliance (evaluating in the frequency domain), but the noisy nature of the observed compliance caused the inversion to fail in nearly every trial.

The inversion's failure at 344A is noteworthy and merits discussion of potential causes. The coupling is particularly complicated here, with coherence banding and frequency-dependent particle motions, which could indicate a subsurface that is too complex to be explained by a simple layer over halfspace model. It is also possible that the infrasound instrument response is not flat and/or deviates from the metadata, as has been noted for some stations in the past (Fee et al., 2023). The choice of prior distributions for each parameter also likely influences the inversion's outcome; priors that deviate significantly from the true subsurface properties could lead to a poor solution. Additionally, low signal–noise on the horizontal channel, improper definition of the true radial direction and limitations of the propagator matrix forward model could also cause unrealistic inversion results. The Poisson solid assumption also merits discussion. In reality, very shallow materials (<30 m) contain varying amounts of air, water, and solids, and can display nonlinear behavior (Oral et al., 2022) and deviate from the Poisson-solid assumption (Brocher, 2005). While this assumption may therefore be imperfect, we adopt it here to simplify the inversion framework and to provide a baseline that can be further refined in the future.

While the inversion scheme has these notable drawbacks, we are encouraged by its ability to reproduce AGCWs reasonably well in diverse coupling scenarios. Future work could build on this foundation in several ways. Exploring alternative inversion methods or refining our existing inversion framework, particularly through improved handling of the likelihood function and more informed prior selection, may yield more physically realistic results. We also pose that, as used in inversion methods with purely seismic Rayleigh waves (Picozzi et al., 2005; Haney and Tsai, 2022), ellipticity (H/V ratio) information could supplement compliance methods to improve the solution. Applying the inversion to the hundreds of TA stations with coupling from Camp Minden (or other places) and comparing results with local geology could be particularity interesting. Similarly, comparing inversion results with quasi-ground-truth subsurface information from active-source seismic surveys (e.g., Edwards et al., 2007) or borehole logs would provide critical validation, ultimately improving confidence in the capability of the method to predict shallow subsurface structure using just a single seismoacoustic sensor pair.

6 Conclusions

We investigate air-to-ground coupled waves (AGCWs) generated by the 2012 Camp Minden Explosion using recordings from seismoacoustic stations of the EarthScope Transportable Array (TA). This explosion was recorded by over 200 stations with colocated sensors. AGCWs arise when acoustic waves (infrasound) couple into the solid Earth, providing valuable insights into both atmospheric sources and near-surface elastic properties. However, interpreting these signals is complicated by their strong sensitivity to subsurface structure.

We quantify seismic particle motion at 126 TA stations using the Normalized Inner-Product, applied in a novel way to AGCWs. This method provides a straightforward, interpretable way to visualize and quantify the particle motion of AGCWs. The results reveal spatially variable particle motions, with prograde motion predominant in low shear-wave velocity regions such as the Mississippi Embayment and retrograde motion more common in higher-velocity regions. Over 30 stations show prograde motion in the 1.5–10 Hz band. These findings support theoretical predictions that prograde motion occurs when the apparent acoustic velocity exceeds the subsurface shear-wave velocity (Bishop et al., 2022), and suggest that prograde motion is more common than previously considered. At some stations, we observe frequency-dependent transitions such as retrograde motion at low frequencies shifting to prograde at higher frequencies, which we interpret as evidence of layered subsurface structures where low velocity sediments overlie more competent material.

We model these observations using a propagator matrix approach with the recorded infrasound to compute acoustic–seismic transfer functions and synthetic seismograms. A Bayesian inversion framework is then applied to constrain subsurface parameters (shear-wave velocity, density, and thickness) for a single-layer-over-halfspace model. Some stations produce physically reasonable shallow subsurface models and achieved good waveform fits (244A, Figure 6; Z43A, Figure 8), whereas at other sites the inversion fails (e.g., 344A, Figure 7), underscoring its limitations.

The significant presence of prograde particle motion in our study is a key observation with implications for all studies of acoustic–seismic coupling and in particular for methods like the Transverse Coherence Minimization (TCM) method (Bishop et al., 2023), which relies on a particle motion assumption to estimate an acoustic back-azimuth. While our Bayesian inversion may not be successful at all seismoacoustic stations, it represents a meaningful step forward to use AGCWs to infer near-surface structure, particularly in cases that require more complexity than a halfspace. Future application and extension of our inversion technique may provide a remote means to quantify the shallow subsurface properties, with implications for station response and seismic hazard characterization.

Acknowledgements

We thank Zongbo Xu for helpful discussions. The authors also thank Toshiro Tanimoto, Alex Iezzi, and an anonymous reviewer for their feedback which helped improve this manuscript. LS, DF, and KM were supported by the Nuclear Arms Control Technology (NACT) program at the Defense Threat Reduction Agency (DTRA) under Contract Number HDTRA121C0030 (Distribution statement: Cleared for release). JB was supported under the Low Yield Nuclear Monitoring (LYNM) program funded by the National Nuclear Security Administration, Defense Nuclear Nonproliferation Research and Development (NNSA DNN R&D). The authors acknowledge important interdisciplinary collaboration with scientists and engineers from LANL, LLNL, NNSS, PNNL, and SNL. Any use of trade, firm, or product names is for descriptive purposes only and does not imply endorsement by the U.S. Government.

Data and code availability

Python code to model air-to-ground coupling with the propagator matrix technique is available on GitHub at https://github.com/uafgeotools/AGCW-PM, and code to compute the NIP is available at https://github.com/uafgeotools/Coupling-NIP. Seismoacoustic waveform data is freely available from the EarthScope IRIS Data Management Center (https://service.iris.edu/; network code TA). The USGS Global V_{S30} Mosaic can be obtained from the USGS Earthquake Hazards Program (https://earthquake.usgs.gov/data/vs30/). We made extensive use of the following Python packages: Obspy (Beyreuther et al., 2010), PyMC (Salvatier et al., 2016), PyGMT (Uieda et al., 2021), and Matplotlib (Hunter, 2007).

Competing interests

The authors have no competing interests.

References

Aki, K. and Richards, P. G. *Quantitative seismology*. MIT Press, 2002.

Albuquerque Seismological Laboratory/USGS. Global Seismograph Network (GSN - IRIS/USGS), 1988. doi: 10.7914/SN/IU.

Anbazhagan, P., Uday, A., Moustafa, S. S. R., and Al-Arifi, N. S. N. Correlation of densities with shear wave velocities and SPT N values. *Journal of Geophysics and Engineering*, 13(3):320–341, 2016. doi: 10.1088/1742-2132/13/3/320.

Anthony, R. E., Ringler, A. T., Tanimoto, T., Matoza, R. S., De Angelis, S., and Wilson, D. C. Earth's Upper Crust Seismically Excited by Infrasound from the 2022 Hunga Tonga–Hunga Ha'apai Eruption, Tonga. *Seismological Research Letters*, 94(2A):603–616, 2022a. doi: 10.1785/0220220252.

Anthony, R. E., Watzak, J., Ringler, A. T., and Wilson, D. C. Characteristics, relationships and precision of direct acoustic-to-seismic coupling measurements from local explosions. *Geophysical Journal International*, 230(3):2019–2035, 2022b. doi: 10.1093/gji/ggac154.

Ben-Menahem and Singh. Seismic Waves and Sources. 1981. doi: 10.1007/978-1-4612-5856-8.

Berg, E. M., Dannemann Dugick, F., Albert, S., and Koch, C. The Strange Case of Ground-Coupled Airwaves on Seismoacoustic Stations at Local to Near-Regional Scales. Technical Report SAND2022-13990, Sandia National Lab. (SNL-NM), Albuquerque, NM (United States), 2022. doi: 10.2172/1891700.

Beyreuther, M., Barsch, R., Krischer, L., Megies, T., Behr, Y., and Wassermann, J. ObsPy: A Python toolbox for seismology. *Seismological Research Letters*, 81(3):530–533, 2010. doi: 10.1785/gssrl.81.3.530.

Bishop, J. W., Fee, D., Modrak, R., Tape, C., and Kim, K. Spectral Element Modeling of Acoustic to Seismic Coupling Over Topography. *Journal of Geophysical Research: Solid Earth*, 127(1): e2021JB023142, 2022. doi: 10.1029/2021JB023142.

Bishop, J. W., Haney, M. M., Fee, D., Matoza, R. S., McKee, K. F., and Lyons, J. J. Back-Azimuth Estimation of Air-to-Ground Coupled Infrasound from Transverse Coherence Minimization. *The Seismic Record*, 3(4):249–258, 2023. doi: 10.1785/0320230023.

Blom, P., Waxler, R., Frazier, W. G., and Talmadge, C. Observations of the refraction of microbaroms generated by large maritime storms by the wind field of the generating storm. *Journal of Geophysical Research: Atmospheres*, 119(12):7179–7192, 2014. doi: 10.1002/2014JD021795.

Brocher, T. M. Empirical Relations between Elastic Wavespeeds and Density in the Earth's Crust. *Bulletin of the Seismological Society of America*, 95(6):2081–2092, 2005. doi: 10.1785/0120050077.

Cansi, Y. An automatic seismic event processing for detection and location: The PMCC method. *Geophysical research letters*, 22(9): 1021–1024, 1995. doi: 10.1029/95GL00468.

Castellaro, S., Mulargia, F., and Rossi, P. L. VS30: Proxy for seismic amplification? *Seismological Research Letters*, 79(4):540–543, 2008. doi: 10.1785/gssrl.79.4.540.

Christensen, N. I. and Mooney, W. D. Seismic velocity structure and composition of the continental crust: A global view. *Journal of Geophysical Research: Solid Earth*, 100(B6):9761–9788, 1995. doi: 10.1029/95JB00259.

Crary, A. and Ewing, M. On a barometric disturbance recorded on a vertical long-period seismograph. *Eos, Transactions American Geophysical Union*, 33(4):499–501, 1952. doi: 10.1029/TR033i004p00499.

De Angelis, S., Fee, D., Haney, M., and Schneider, D. Detecting hidden volcanic explosions from Mt. Cleveland Volcano, Alaska with infrasound and ground-coupled airwaves. *Geophysical Research Letters*, 39(21), 2012. doi: 10.1029/2012GL053635.

de Groot-Hedlin, C. D. and Hedlin, M. A. Infrasound detection of the Chelyabinsk meteor at the USArray. *Earth and Planetary Science Letters*, 402:337–345, 2014. doi: 10.1016/j.epsl.2014.01.031.

Edwards, W. N., Eaton, D. W., McCausland, P. J., ReVelle, D. O., and Brown, P. G. Calibrating infrasonic to seismic coupling using the Stardust sample return capsule shockwave: Implications for seismic observations of meteors. *Journal of Geophysical Research: Solid Earth*, 112(B10), 2007. doi: 10.1029/2006JB004621.

Ewing, M. and Press, F. Further study of atmospheric pressure fluctuations recorded on seismographs. *Eos, Transactions American Geophysical Union*, 34(1):95–100, 1953. doi: 10.1029/TR034i001p00095.

Fee, D. and Matoza, R. S. An overview of volcano infrasound: From hawaiian to plinian, local to global. *Journal of Volcanology and Geothermal Research*, 249:123–139, 2013. doi: 10.1016/j.jvolgeores.2012.09.002.

Fee, D., Haney, M., Matoza, R., Szuberla, C., Lyons, J., and Waythomas, C. Seismic envelope-based detection and location of ground-coupled airwaves from volcanoes in Alaska. *Bulletin of the Seismological Society of America*, 106(3):1024–1035, 2016. doi: 10.1785/0120150244.

Fee, D., Macpherson, K., and Gabrielson, T. Characterizing Infrasound Station Frequency Response Using Large Earthquakes and Colocated Seismometers. *Bulletin of the Seismological Society of America*, 113(4):1581–1595, 2023. doi: 10.1785/0120220226.

Fee, D., Tan, D., Haney, M., Merritt, K., Lyons, J., Wech, A., Loewen, M., Boyce, E., and Scamfer, L. Seismic and infrasound signals from the 2023 explosive eruption sequence of Shishaldin Volcano, Alaska. *Bulletin of Volcanology*, in press. doi: 10.1007/s00445-026-01951-351.

Godin, O. A. Shear waves and sound attenuation in underwater waveguides. *The Journal of the Acoustical Society of America*, 149(5):3586–3598, 2021. doi: 10.1121/10.0004999.

Haney, M. M. and Tsai, V. C. Rayleigh-wave ellipticity in weakly heterogeneous layered media. *Geophysical Journal International*, 228(2):1313–1323, 2022. doi: 10.1093/gji/ggab395.

Harkrider, D. G. and Flinn, E. A. Effect of crustal structure on rayleigh waves generated by atmospheric explosions. *Reviews of Geophysics*, 8(3):501–516, 1970. doi: 10.1029/RG008i003p00501.

Haskell, N. A. The dispersion of surface waves on multilayered media*. *Bulletin of the Seismological Society of America*, 43(1): 17–34, 1953. doi: 10.1785/BSSA0430010017.

Haubrich, R. A. and MacKenzie, G. S. Earth noise, 5 to 500 millicycles per second: 2. Reaction of the Earth to oceans and atmosphere. *Journal of Geophysical Research (1896-1977)*, 70(6): 1429–1440, 1965. doi: 10.1029/JZ070i006p01429.

Heath, D. C., Wald, D. J., Worden, C. B., Thompson, E. M., and Smoczyk, G. M. A global hybrid VS30 map with a topographic slope–based default and regional map insets. *Earthquake Spectra*, 36(3):1570–1584, 2020. doi: 10.1177/8755293020911137.

Herrmann, R. B. Computer programs in seismology: An evolving tool for instruction and research. *Seismological Research Letters*, 84(6):1081–1088, 2013. doi: 10.1785/0220110096.

Hicks, S. P., Matos, S. B., Pimentel, A., Belli, G., Gheri, D., Tsekhmistrenko, M., Hosseini, K., Geissler, W. H., Silva, R., Wallenstein, N., and Ferreira, A. M. G. Exclusive Seismoacoustic Detection and Characterization of an Unseen and Unheard Fireball Over the North Atlantic. *Geophysical Research Letters*, 50(22): e2023GL105773, 2023. doi: 10.1029/2023GL105773.

Hirose, T. and Ueda, H. Seismic wavefield change preceding the eruption of Shinmoe-dake, Kirishima volcano, Japan, inferred from polarization analysis. *Journal of Geophysical Research: Solid Earth*, 130(3):e2024JB029358, 2025. doi: 10.1029/2024JB029358.

Hunter, J. D. Matplotlib: A 2D Graphics Environment. *Computing in Science & Engineering*, 9(3):90–95, 2007. doi: 10.1109/MCSE.2007.55.

Ichihara, M., Takeo, M., Yokoo, A., Oikawa, J., and Ohminato, T. Monitoring volcanic activity using correlation patterns between infrasound and ground motion. *Geophysical Research Letters*, 39(4), 2012. doi: 10.1029/2011GL050542.

Jardetzky, W. S. and Press, F. Rayleigh-wave coupling to atmospheric compression waves*. *Bulletin of the Seismological Society of America*, 42(2):135–144, 1952. doi: 10.1785/BSSA0420020135.

Langston, C. A. Seismic ground motions from a bolide shock wave. *Journal of Geophysical Research: Solid Earth*, 109(B12), 2004.

doi: 10.1029/2004JB003167.

Liu, H.-P., Hu, Y., Dorman, J., Chang, T.-S., and Chiu, J.-M. Upper Mississippi embayment shallow seismic velocities measured in situ. *Engineering Geology*, 46(3):313–330, 1997. doi: 10.1016/S0013-7952(97)00009-4.

Macpherson, K., Fee, D., Awender, S., Chow, B., Colwell, J., Delamere, S., and Haney, M. Alaska Upper Crustal Velocities Revealed by Air-to-Ground Coupled Waves From the 2022 Hunga Tonga-Hunga Ha'apai Eruption. *Seismica*, 4(2), 2025. doi: 10.26443/seismica.v4i2.1557.

Matoza, R. S. and Fee, D. Infrasonic component of volcano-seismic eruption tremor. *Geophysical Research Letters*, 41(6): 1964–1970, 2014. doi: 10.1002/2014GL059301.

McKee, K., Fee, D., Haney, M., Matoza, R. S., and Lyons, J. Infrasound Signal Detection and Back Azimuth Estimation Using Ground-Coupled Airwaves on a Seismo-Acoustic Sensor Pair. *Journal of Geophysical Research: Solid Earth*, 123(8):6826–6844, 2018. doi: 10.1029/2017JB015132.

McPherson, A. M., Tape, C., Fee, D., Thurin, J., and Bishop, J. W. Estimating an airborne dipole source using 3-D wavefield simulations and seismic receivers on the ground. *Geophysical Journal International*, 244(3), 2026. doi: 10.1093/gji/ggaf499.

Meltzer, A., Rudnick, R., Zeitler, P., Levander, A., Humphreys, G., Karlstrom, K., Ekstrom, E., Carlson, C., Dixon, T., and Gurnis, M. The usarray initiative. *Geological Society of America Today*, 9: 8–10, 1999.

Meza-Fajardo, K. C., Papageorgiou, A. S., and Semblat, J. Identification and Extraction of Surface Waves from Three-Component Seismograms Based on the Normalized Inner Product. *Bulletin of the Seismological Society of America*, 105(1):210–229, 2015. doi: 10.1785/0120140012.

Mori, F., Mendicelli, A., Moscatelli, M., Romagnoli, G., Peronace, E., and Naso, G. A new Vs30 map for Italy based on the seismic microzonation dataset. *Engineering Geology*, 275:105745, 2020. doi: 10.1016/j.enggeo.2020.105745.

Nippress, A. and Green, D. N. Global empirical models for infrasonic celerity and backazimuth. *Geophysical Journal International*, 235(2):1912–1925, 2023. doi: 10.1093/gji/ggad334.

Novoselov, A., Fuchs, F., and Bokelmann, G. Acoustic-to-seismic ground coupling: coupling efficiency and inferring near-surface properties. *Geophysical Journal International*, 223(1):144–160, 2020. doi: 10.1093/gji/ggaa304.

Oral, E., Ayoubi, P., Ampuero, J. P., Asimaki, D., and Bonilla, L. F. Kathmandu Basin as a local modulator of seismic waves: 2-D modelling of non-linear site response under obliquely incident waves. *Geophysical Journal International*, 231(3):1996–2008, 2022. doi: 10.1093/gji/ggac302.

Picozzi, M., Parolai, S., and Richwalski, S. M. Joint inversion of H/V ratios and dispersion curves from seismic noise: Estimating the S-wave velocity of bedrock. *Geophysical Research Letters*, 32 (11), 2005. doi: 10.1029/2005GL022878.

Press, F. and Ewing, M. Ground roll coupling to atmospheric compressional waves. *Geophysics*, 16(3):416–430, 1951. doi: 10.1190/1.1437684.

Romero, S. and Rix, G. J. Regional variations in near surface shear wave velocity in the Greater Memphis area. *Engineering Geology*, 62(1):137–158, 2001. doi: 10.1016/S0013-7952(01)00059-X.

Salvatier, J., Wiecki, T. V., and Fonnesbeck, C. Probabilistic programming in Python using PyMC3. *PeerJ Computer Science*, 2: e55, 2016. doi: 10.7717/peerj-cs.55.

Sanderson, R. W., Matoza, R. S., Fee, D., Haney, M. M., and Lyons, J. J. Remote Detection and Location of Explosive Volcanism in Alaska With the EarthScope Transportable Array. *Journal of Geophysical Research: Solid Earth*, 125(4):e2019JB018347, 2020. doi: 10.1029/2019JB018347.

Savran, W. and Olsen, K. Model for small-scale crustal heterogeneity in Los Angeles basin based on inversion of sonic log data. *Geophysical Journal International*, 205(2):856–863, 2016. doi: 10.1093/gji/ggw050.

Seppi, I., Tape, C., and Fee, D. Classification of Aircraft Types Using Seismic Data in Alaska. *The Seismic Record*, 5(4):330–340, 2025. doi: 10.1785/0320250035.

Sorrells, G. G. A Preliminary Investigation into the Relationship between Long-Period Seismic Noise and Local Fluctuations in the Atmospheric Pressure Field. *Geophysical Journal International*, 26(1-4):71–82, 1971. doi: 10.1111/j.1365-246X.1971.tb03383.x.

Szuberla, C. A. and Olson, J. V. Uncertainties associated with parameter estimation in atmospheric infrasound arrays. *The Journal of the Acoustical Society of America*, 115(1):253–258, 2004. doi: 10.1121/1.1635407.

Tanimoto, T. Deformation of solid earth by surface pressure: equivalence between Ben-Menahem and Singh's formula and Sorrells' formula. *Geophysical Journal International*, 238(2): 820–826, 2024. doi: 10.1093/gji/ggae185.

Tanimoto, T. Normal Modes in a Coupled Earth Model: A New Perspective on the Compliance Method. *Journal of Geophysical Research: Solid Earth*, 131(4):e2025JB032779, 2026. doi: 10.1029/2025JB032779.

Tanimoto, T. and Rivera, L. Prograde Rayleigh wave particle motion. *Geophysical Journal International*, 162(2):399–405, 2005. doi: 10.1111/j.1365-246X.2005.02481.x.

Tanimoto, T. and Wang, J. Low-Frequency Seismic Noise Characteristics From the Analysis of Co-Located Seismic and Pressure Data. *Journal of Geophysical Research: Solid Earth*, 123(7): 5853–5885, 2018. doi: 10.1029/2018JB015519.

Tanimoto, T. and Wang, J. Theory for deriving shallow elasticity structure from colocated seismic and pressure data. *Journal of Geophysical Research: Solid Earth*, 124(6):5811–5835, 2019. doi: 10.1029/2018JB017132.

Tanimoto, T. and Wang, J. Shallow elasticity structure from colocated pressure and seismic stations in the Piñon Flat Observatory and estimation of Vs30. *Geophysical Journal International*, 222(1):678–696, 2020. doi: 10.1093/gji/ggaa195.

Uieda, L., Tian, D., Leong, W. J., Toney, L., Schlitzer, W., Grund, M., Newton, D., Ziebarth, M., Jones, M., and Wessel, P. PyGMT: A Python interface for the generic mapping tools. 2021. doi: 10.5281/zenodo.5607255.

U.S. Department of Justice. Explo officials sentenced for roles in conspiracy that led to illegal dumping of munitions and explosion at Camp Minden. Press Release, Nov. 2018. https://www.justice.gov/usao-wdla/pr/explo-officials-sentenced-roles-conspiracy-led-illegal-dumping-munitions-and-explosion-at-camp-minden. Updated November 29, 2018.

Vergoz, J., Hupe, P., Listowski, C., Le Pichon, A., Garcés, M. A., Marchetti, E., Labazuy, P., Ceranna, L., Pilger, C., Gaebler, P., Näsholm, S. P., Brissaud, Q., Poli, P., Shapiro, N., De Negri, R., and Mialle, P. IMS observations of infrasound and acoustic-gravity waves produced by the January 2022 volcanic eruption of Hunga, Tonga: A global analysis. *Earth and Planetary Science Letters*, 591:117639, 2022. doi: 10.1016/j.epsl.2022.117639.

Wald, D. J. and Allen, T. I. Topographic Slope as a Proxy for Seismic Site Conditions and Amplification. *Bulletin of the Seismological Society of America*, 97(5):1379–1395, 2007. doi: 10.1785/0120060267.

Walker, K. T., Hedlin, M. A. H., de Groot-Hedlin, C., Vergoz, J., Le Pichon, A., and Drob, D. P. Source location of the 19 February

2008 Oregon bolide using seismic networks and infrasound arrays. *Journal of Geophysical Research: Solid Earth*, 115(B12), 2010. doi: 10.1029/2010JB007863.

Wang, J. and Tanimoto, T. Estimating Near-Surface Rigidity from Low-Frequency Noise Using Collocated Pressure and Horizontal Seismic Data. *Bulletin of the Seismological Society of America*, 110(4):1960–1970, 2020. doi: 10.1785/0120200098.

Wang, T., Wang, Y., Xue, Q., Zheng, Y., and Lu, H. The seismic responses and its Doppler effects of moving aircraft caused by acoustic-seismic coupling. *IEEE Transactions on Geoscience and Remote Sensing*, 62:1–12, 2024. doi: 10.1109/TGRS.2024.3358582.

Whitaker, R. W. and Mutschlecner, J. P. A comparison of infrasound signals refracted from stratospheric and thermospheric altitudes. *Journal of Geophysical Research: Atmospheres*, 113 (D8), 2008. doi: 10.1029/2007JD008852.

Wills, G., Nippress, A., Green, D. N., and Spence, P. J. Site-specific variations in air-to-ground coupled seismic arrivals from the 2012 October 16 explosion at Camp Minden, Louisiana, United States. *Geophysical Journal International*, 231(1):243–255, 2022. doi: 10.1093/gji/ggac184.

Xu, Z. and Lognonné, P. A comprehensive theory for 1-D (an)elastic medium deformation due to plane-wave fluid pressure perturbation. *Geophysical Journal International*, 236(3):1499–1512, 2024. doi: 10.1093/gji/ggae005.

Zhou, J., Li, L., Li, X., Yu, Y., and Tian, Q. Lateral variations of shear wave velocity (*V*S) profile and *V*S30 over gentle terrain. *Soil Dynamics and Earthquake Engineering*, 175:108265, 2023. doi: 10.1016/j.soildyn.2023.108265.